Geomorphology 214 (2014) 339–355

Contents lists available at ScienceDirect

Geomorphology

journal homepage: www.elsevier.com/locate/geomorph

The evaluation of unmanned aerial system-based photogrammetry and terrestrial laser scanning to generate DEMs of agricultural watersheds

Mohamar Moussa Ouédraogo [a,*], Aurore Degré [a], Charles Debouche [a], Jonathan Lisein [b]

[a] Systèmes Sol-Eau, Gembloux Agro-Bio Tech, Université de Liège, Passage des Déportés 2, Gembloux, Belgium
[b] Gestion des Ressources Forestières et des Milieux naturels, Gembloux Agro-Bio Tech, Université de Liège, Passage des Déportés 2, Gembloux, Belgium

ARTICLE INFO

Article history:
Received 8 January 2013
Received in revised form 13 February 2014
Accepted 23 February 2014
Available online 1 March 2014

Keywords:
DEM
Terrestrial laser scanning
UAS
Agricultural watershed
Errors

ABSTRACT

Agricultural watersheds tend to be places of intensive farming activities that permanently modify their microtopography. The surface characteristics of the soil vary depending on the crops that are cultivated in these areas. Agricultural soil microtopography plays an important role in the quantification of runoff and sediment transport because the presence of crops, crop residues, furrows and ridges may impact the direction of water flow. To better assess such phenomena, 3-D reconstructions of high-resolution agricultural watershed topography are essential. Fine-resolution topographic data collection technologies can be used to discern highly detailed elevation variability in these areas. Knowledge of the strengths and weaknesses of existing technologies used for data collection on agricultural watersheds may be helpful in choosing an appropriate technology. This study assesses the suitability of terrestrial laser scanning (TLS) and unmanned aerial system (UAS) photogrammetry for collecting the fine-resolution topographic data required to generate accurate, high-resolution digital elevation models (DEMs) in a small watershed area (12 ha). Because of farming activity, 14 TLS scans (≈25 points m^{-2}) were collected without using high-definition surveying (HDS) targets, which are generally used to mesh adjacent scans. To evaluate the accuracy of the DEMs created from the TLS scan data, 1098 ground control points (GCPs) were surveyed using a real time kinematic global positioning system (RTK-GPS). Linear regressions were then applied to each DEM to remove vertical errors from the TLS point elevations, errors caused by the non-perpendicularity of the scanner's vertical axis to the local horizontal plane, and errors correlated with the distance to the scanner's position. The scans were then meshed to generate a DEM_{TLS} with a 1 × 1 m spatial resolution. The Agisoft PhotoScan and MicMac software packages were used to process the aerial photographs and generate a DEM_{PSC} (Agisoft PhotoScan) and DEM_{MCM} (MicMac), respectively, with spatial resolutions of 1 × 1 m. Comparing the DEMs with the 1098 GCPs showed that the DEM_{TLS} was the most accurate data product, with a root mean square error (*RMSE*) of 4.5 cm, followed by the DEM_{MCM} and the DEM_{PSC}, which had *RMSE* values of 9.0 and 13.9 cm, respectively. The DEM_{PSC} had absolute errors along the border of the study area that ranged from 15.0 to 52.0 cm, indicating the presence of systematic errors. Although the derived DEM_{MCM} was accurate, an error analysis along a transect showed that the errors in the DEM_{MCM} data tended to increase in areas of lower elevation. Compared with TLS, UAS is a promising tool for data collection because of its flexibility and low operational cost. However, improvements are needed in the photogrammetric processing of the aerial photographs to remove non-linear distortions.

1. Introduction

Digital elevation models (DEMs) are among the most important spatial information tools used in geomorphological applications because they allow for the extraction of crucial attributes, such as slope, aspect, profile curvature, and flow direction. Elevation data can be acquired from three main sources (Nelson et al., 2009): (1) ground surveys (Peucker et al., 1978; Niewinski, 2004); (2) existing topographic maps (Gooch et al., 1999; Henry et al., 2002; Fabris and Pesci, 2005; Hladik and Alber, 2012); and (3) remote sensing (Huising and Gomes Pereira, 1998; Wehr and Lohr, 1999; Eisenbeiss and Zhang, 2006; Guarnieri et al., 2009; Höhle, 2009). Although ground survey techniques are very accurate compared with topographic maps and remote sensing, the data acquisition can be time-consuming when the applications require high-resolution DEMs. Remote sensing technologies, including airborne photogrammetry and satellite photogrammetry, interferometry, and light detection and ranging (LiDAR) techniques, can be costly for areas of only a few km^2 (Eisenbeiss, 2009). The rapid development of technology over the past few years has seen the emergence of new, flexible, fine-resolution topographic data collection technologies, such

* Corresponding author. Tel.: +32 81 62 22 41; fax: +32 81 62 23 16.
E-mail address: mohamarmoussa.ouedraogo@ulg.ac.be (M.M. Ouédraogo).

http://dx.doi.org/10.1016/j.geomorph.2014.02.016
0169-555X/

as terrestrial laser scanning (TLS) and unmanned aerial system (UAS) photogrammetry.

1.1. Use of DEMs in agriculture

Several approaches have been used to generate DEMs for agricultural applications. DEMs can be generated from handheld high-resolution cameras located a few meters above ground level. This technique was assessed by Warner (1995) on a 1 m^2 plowed field. He suggested that this method was suitable for mapping tilled soil over areas of a few square meters and did not require any photogrammetric experience, although it is less precise than traditional close-range photogrammetry. This technique has been widely used in many studies to assess agricultural soil erosion and deposition (Yang et al., 2009; Gessesse et al., 2010), quantifying water storage on soil surfaces (Bogner et al., 2013), identifying and characterizing clods (Taconet et al., 2010), assessing gully locations (Svoray and Markovitch, 2009) and determining agricultural soil roughness (Taconet and Ciarletti, 2007). Other techniques used to generate agricultural soil DEMs include using contour lines to calculate potential surface runoff (Rosatto et al., 2011), DGPS (Differential Global Positioning System) for mapping grain and straw (Reyniers et al., 2006), laser tachometry for quantifying and explaining the origin of the morphological and geochemical properties of soil that has accumulated in terraces (Salvador-Blanes et al., 2006), profile laser scanning for clod detection (Hammad et al., 2006), and TLS, which is an emerging technology for characterizing soil tillage characteristics at very high resolutions (Barneveld et al., 2013).

Most of the applications mentioned here used DEMs that were only a few square meters in area and that were located mainly on one plot. However, applications (e.g., runoff pathway extraction, and basin delineation) often require DEMs of an entire watershed of a few hectares that comprises several plots, so it is necessary to use technologies that have the flexibility to produce high-resolution DEMs over several hectares, such as TLS and UAS photogrammetry.

1.2. Terrestrial laser scanning

The TLS technique involves sending and receiving laser pulses to build a point file of 3D coordinates of the scanned surface. The time of travel for a single pulse reflection is measured along a known trajectory and allows the distance from the laser, and consequently the position of the point of interest, to be computed. Using this methodology, data collection occurs at a rate of thousands of points per second and generates a point cloud of 3D coordinates.

TLS has been used for a variety of applications, including structural monitoring (Brinkman and O'Neill, 2000; Gordon et al., 2003; Smith, 2005; Guarnieri et al., 2006; Landes and Grussenmeyer, 2011), recording cultural heritage (Vozikis et al., 2004; Jütte, 2008; Kersten et al., 2008; Eisenbeiss, 2009; Goulette, 2009; Herbin, 2012), landslide monitoring (Aber et al., 2002; Fotinopoulos, 2004; Gonzalez-Aguilera and Gomez-Lahoz, 2009) and forensic characterization (Webster and Olivier, 2007; Zhang, 2008; Haala et al., 2011). With ongoing technological improvements, the field of TLS has expanded, and many studies have used TLS data to generate DEMs (Mitas and Mitasova, 1999; Lane et al., 2000; Hirano et al., 2003; Guarnieri et al., 2009; Coveney et al., 2010; Perroy et al., 2010; Coveney and Fotheringham, 2011; Smith et al., 2011; Eitel et al., 2011a; Barneveld et al., 2013).

Although many studies have investigated agricultural fields to model crop growth (Eitel et al., 2010, 2011b; Ehlert and Heisig, 2013), few have assessed the suitability of TLS data for generating DEMs of agricultural soil surfaces (Barneveld et al., 2013), and there is a lack of research at the watershed scale. Such data, however, could provide high-resolution, accurate DEMs for hydrological process modeling. In particular many agricultural watersheds are facing intense farming activities that change the microtopography of the land and make them very difficult to accurately model.

An agricultural watershed area generally contains more than one plot. Depending on the time of year, plots differ in soil structure and cover, which can change their topography. Many studies have reported that the most relevant characteristics of agricultural soil surfaces, such as crusting (Cerdan et al., 2002; Le Bissonnais et al., 2005; Carmi and Berliner, 2008; Rodríguez-Caballero et al., 2012), roughness (Takken et al., 2001a,b; Rai et al., 2010; Zhao et al., 2013), and crop and crop residue cover (Wilson et al., 2008; Sasal et al., 2010) affect infiltration, temporary storage capacity, runoff rates and direction, and erosion. The ability of TLS to produce high-resolution DEMs that are capable of resolving individual ridges and depressions is particularly useful for the detailed surface characterization and micro-scale hydrological modeling necessary to determine the runoff direction. The presence of crops and crop residues on agricultural plots and the effect of tillage on soil structure, however, can make the data collection difficult and make the data have questionable value. It is therefore debatable whether TLS technology is suitable for collecting and analyzing data to be used for the creation of DEMs of agricultural watersheds.

1.3. UAS photogrammetry

The use of stereoscopic aerial photographic pairs for generating DEMs has been extensively investigated — see Gruen (2012) for a review of the development of image-matching since 1960. Nevertheless, the method is constrained by the price and flexibility of traditional aerial surveys (manned aircraft), which are unsuitable for surveying small areas (± 1 km^2). The recent use of UASs in geomatics offers a cost-effective way to produce aerial imagery at very high spatial and temporal resolutions. Examples of UASs include motorized paragliders (Jütte, 2008), blimps (Ries and Marzolff, 2003; Gonzalez-Aguilera and Gomez-Lahoz, 2009), kites (Smith et al., 2009), balloons (Fotinopoulos, 2004), fixed-wing UASs (Haala et al., 2011; Kung et al., 2011) and rotary-wing UASs (Zhang, 2008; Niethammer et al., 2010). The expected ground pixel spatial resolution can be less than 10×10 cm, and only small investments of time and money are required for small studies. In addition, the flexibility of UASs enables a time series of aerial photographs to be acquired and used to detect changes in microtopography that can affect hydrological processes (e.g., soil runoff). With small human interventions, i.e., the designation of several ground control points (GCPs) in the images, an accuracy of 0.05–0.20 cm can be achieved (Kung et al., 2011).

Although the use of rapid terrain mapping tools such as micro-UASs is very promising (Hardin and Jensen, 2011), many issues persist when mini-UAS photogrammetry techniques are used for scientific purposes; for details about UAS classification, see Watts et al. (2012). Recent progress in computer vision, photogrammetry and computing power has led to an operational solution for 3D data acquisition that is based on structure-from-motion photogrammetry, which is also referred to as structure-from-motion-multi-view stereo (Snavely et al., 2008; James and Robson, 2012; Westoby et al., 2012; Fonstad et al., 2013). However, there is still no robust, harmonized methodology for acquiring and processing images. The bottleneck occurs mainly in the process chain, which greatly depends on the software used (and thus, indirectly, on the algorithm) and has a significant influence on the resulting accuracy.

The accuracy of these approaches needs to be investigated further, especially in relation to agricultural watersheds where the soil roughness and texture vary due to farming activity. Although many studies have focused on the accuracy of DEM-based photogrammetry, only a few applications (Eisenbeiss, 2009; Kung et al., 2011; Vallet et al., 2011; James and Robson, 2012; Westoby et al., 2012; Fonstad et al., 2013) have used UAS images because this technology is so new.

1.4. Goal of this article

High-resolution digital elevation models of agricultural watersheds can be helpful for analyzing the impact of agricultural soil roughness from tillage, crops and crop residues on geomorphological parameters.

Therefore, the first aim of this study is to produce a high-resolution DEM of a small agricultural watershed using elevation data from two emerging fine-resolution topographic data collection technologies: TLS and UAS photogrammetry. The second aim is to assess the accuracy, strengths and weaknesses of each method by comparing the generated DEMs with ground control points and by highlighting their specific characteristics. Such comparisons should be helpful for users in choosing the appropriate method for generating high-resolution DEMs of agricultural watersheds.

2. Material and methods

2.1. Study site

The study site is an easily accessible small watershed (12 ha) in Wallonia, Belgium (Fig. 1). The watershed is free of any human activities apart from farming and is comprised entirely of agricultural plots. The mean elevation is 165 m, and the minimum and maximum elevations are 159 and 169 m, respectively. The area is relatively flat with a mean slope of 3.67%. The soil is loamy with textural and structural B horizons. The drainage varies from moderately well-drained to well-drained.

2.2. Data surveying

2.2.1. Ground control points (GCPs)

A total of 1098 points were surveyed across the surface of the watershed from April 2008 to September 2009, and all these points were retained to assess the DEM's accuracy. The points were approximately 10 m apart on a regular grid, and the data were collected using a Leica GPS1200 GPS in static RTK mode on the bare surface. This mode gives highly accurate coordinates of points that can be used to assess the accuracy of less accurate data. The Leica GPS1200 has a nominal accuracy of 1 cm for the *x* and *y* coordinates and 1.5 cm for the *z* coordinate (Leica Geosystems, 2008). All the coordinates were surveyed in the Belgian Datum 1972 projection system. The plots had also been plowed prior to data collection.

2.2.2. TLS surveying

Data collection on the agricultural watershed using TLS was a delicate operation because the watershed comprised several plots owned by different farmers. To collect the elevation data, we had to wait until the crops had been harvested to ensure that the surface was bare or that the crops were no higher than ± 10 cm. In addition, harvesting crops from the same plot could take several days or several weeks, depending on the weather and the farmer's activities. Thus, the data were collected each time the plot or a portion of its surface was bare. This led to individual scans being performed without using any TLS mesh targets that could be used to link subsequent scans, as was done in other studies (Perroy et al., 2010; Coveney and Fotheringham, 2011). Fourteen overlapping TLS scans obtained from fourteen stations numbered from ST1 to ST14 (Fig. 2) were needed to cover the entire surface of the watershed. The differences in soil tillage across the watershed are illustrated in Fig. 3. Table 1 shows the soil tillage and the number of points within each scan.

Nine scan stations were initially planned in ArcGIS to obtain the *x* and *y* coordinates for a scanning range of 100 m. Due to 'shadow zones', however, we had to add five more stations to cover the area of interest. A Leica GPS1200 was used in the RTK mode to locate the stations on the plots. Two high-definition surveying (HDS) targets were also surveyed with the Leica GPS1200 for each scan to ensure that the scanning cloud would be in the correct projection system of Belgian Datum 1972. The scanning was conducted with a Trimble Gx TLS scanner using the PointScape (v3.1) software. The Trimble Gx uses a class 2 pulsed 532 nm green laser with a standard distance range of 200 m. Its field of view is limited to 360° × 60°, with an asymmetric vertical portion that is approximately 40° above the horizon. The device's scanning speed is up to 5000 points per second, and it operates in a single-return laser pulse mode that can capture survey points at an accuracy of 12 mm within a data capture range of 100 m. Scanning was performed from a tripod that ranged from 1.8 to 2.0 m high. The scanning resolution (mean distance between points) was set at 20 cm, which corresponded to an approximate point density of ± 25 points m^{-2}.

2.2.3. Photogrammetry surveying

In this study, we used a small Gatewing X100 UAS (wingspan: 100 cm; weight with payload: 2 kg; cruise speed: 80 km h^{-1}; flight height: 100–750 m; maximum flight duration: 40 min). The X100 (see http://www.gatewing.com/X100 for images) is a fixed-wing system that is equipped with a GPS and an inertial measurement unit (IMU). Its flights are completely autonomous from takeoff to landing, and the flight plan is defined beforehand by setting the flight parameters (scanning zone, image overlap, flight altitude, and takeoff and landing location). The ground control station consists of a rugged tablet computer (Yuma Trimble®) that maintains constant contact with the UAS and allows the remote pilot to interrupt the flight in case of an accident hazard. The effective range of this UAS is up to 2 km, and its flight endurance is long enough for it to cover 100 ha at 100 m above ground level. The X100 uses a catapult launcher for takeoff and requires a 150 × 30 m landing strip that is clear of any obstacles. Its optical sensor is a consumer grade camera (Ricoh GR Digital III) with a charged couple device (CCD) of 10 megapixel resolution and a fixed focal length of 6 mm (either 28 or 35 mm equivalent focal length).

Given that the TLS data must be used for other applications, the Ricoh camera was adapted for near-infrared (NIR) acquisition by removing its red blocking filter and fitting it with a yellow filter (for more information, see Verhoeven, 2008 and Hunt et al., 2010); this

Fig. 1. Orthophotograph of the study site that is located at 50°34′33.00″N and 4°39′50.75″E, in the WGS84 reference system. (Source: Service Public de Wallonie, Direction Générale Opérationnelle Agriculture, Ressources Naturelles et Environnement).

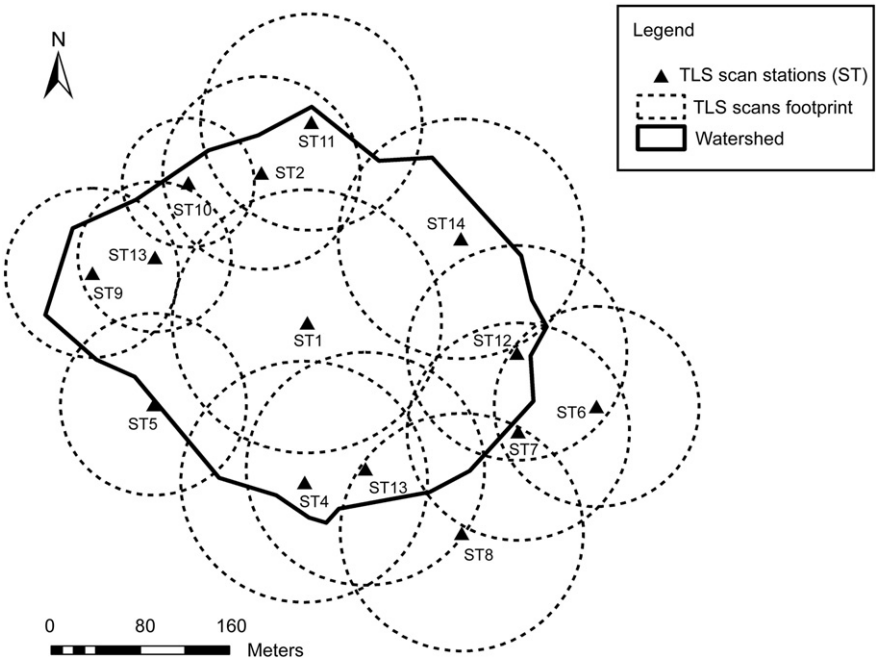

Fig. 2. TLS station footprints on the watershed.

modification did not impact the image processing. The aerial survey was launched on 13 October 2011 under clear skies and moderate wind conditions. Flight authorization was given by the Belgian Civil Aviation Authority. The flight was conducted at a maximum of 100 m above ground level, which corresponds to a pixel spatial resolution (ground sample distance) of 3.3 × 3.3 cm. The pictures were taken with forward and side overlaps of 80%, which is equivalent to a distance of 25 m between two adjacent images. Ten GCPs were manually placed on the study site and surveyed using a Leica GPS1200 to precisely georeference the resulting DEMs. When the flights were performed, wheat had just been harvested from the plots, except for a small area that was cultivated with a mustard crop ranging in height from ±10 to ±20 cm (Fig. 4).

2.3. Data processing

2.3.1. DEM computation and error analysis from TLS data

The 14 scans obtained from the field operations were manually processed in Trimble RealWorks v7 to delete points outside the area of interest. These points were mainly from buildings and trees surrounding the study site. The scan point coordinates (X_{TLS}, Y_{TLS}, Z_{TLS} in Belgian Datum Lambert 72) were exported in a text file for analysis. To compare the scans with the GCPs for error analysis, a raster DEM was computed from each scan in ArcGIS, using the method described by Guarnieri et al. (2009). The method involved selecting as a pixel value the minimum TLS point elevation within a moving window of a fixed size, which corresponded to the final DEM's spatial resolution. This procedure ensured the selection of a point with a high probability of ground return because the agricultural plots were not free of crops (<10 cm) or crop residues. The window size used in this study was set at 1 m.

We considered the DEM error to be the difference between the given value of a pixel and the true value (Wechsler, 2007). To determine whether a DEM contains errors, the field observations (also referred to as 'true values') must be more accurate than the data collected for the DEM generation. The GCPs were used as references. For a DEM generated from the scan data, the errors are defined by:

$$E_i = Z_{GCP} - Z_{DEM} \quad (i = 1 \ldots n) \tag{1}$$

where n is the number of GCPs on the scan footprint, Z_{GCP} corresponds to the elevation of the i-th GCP, and Z_{DEM} is the elevation of the i-th pixel.

According to the U.S. Geological Survey (1997), DEM errors are generally divided into three groups: systematic, blunders or random. If data have been well reviewed before DEM generation, it can be assumed that blunders have largely been removed. In this case, the DEM error can be considered to be the sum of only systematic and random errors.

Fig. 3. Soil tillage on the plots during scanning. (A) Tilled using a moldboard plow (Soil A); the soil surface was free from any crops or crop residues. (B) Tilled using a disk harrow after the wheat harvest (Soil B); the soil surface was covered by crop residues and grass less than 10 cm high. (C) A plot after the sugar beet harvest (Soil C).

Table 1
Soil tillage differences during the scanning operations and the number of points within each scan.

Stations	Number of points within scans	Plot tillage
ST1	185,797	Plowed
ST2	126,798	Plowed
ST3	107,126	Plowed
ST4	150,389	Plowed
ST5	170,852	Plowed
ST6	112,472	After beet harvest
ST7	23,791	After beet harvest
ST8	133,867	After beet harvest
ST9	76,691	Grass (<10 cm)
ST10	61,784	Grass (<10 cm)
ST11	89,180	Grass (<10 cm)
ST12	99,112	Grass (<10 cm)
ST13	58,251	Grass (<10 cm)
ST14	200,852	Grass (<10 cm)

Systematic errors result from the procedures used to generate the DEM and follow fixed patterns that can cause bias or artifacts in the final DEM. When the cause of a systematic error is known, the error can be removed or reduced. Random errors are those that remain in the data when systematic errors and blunders have been removed. Assuming that blunders have been removed from the data, the DEM error can be modeled:

$$E = e + R \tag{2}$$

where E is a random variable that represents all errors, e denotes the systematic error, and R is a random variable that represents the random error.

Given that the structure of agricultural soil is continuously modified by farming activities, setting up the tripod on certain plots was difficult, and the scanner's vertical axis may have moved during the scanning operation, meaning that it might not have been perpendicular to the local horizontal plane. Any change to the Trimble Gx's vertical axis during scanning would have introduced errors in the surveyed points' elevations. Assuming that those spatial errors are linearly correlated with the x and y coordinates, it is possible to detect them in the elevation data of a scan by applying a multivariate linear regression on E_i. The independent variable is e_1, and the dependent variables are x and y, which correspond to the coordinates of the errors. Then, e_1 is modeled by the linear relationship

$$e_1 = ax + by + c \tag{3}$$

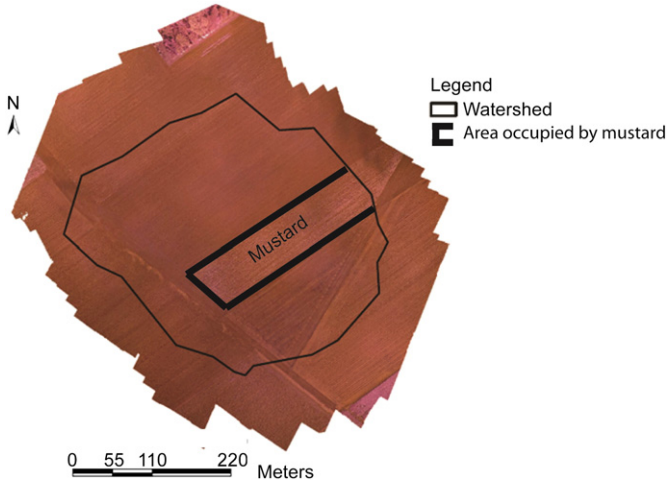

Fig. 4. Location of area cultivated with mustard during the aerial photograph collection with Gatewing X100 UAS.

where a, b and c are constant. The known relationship describing e_1 is used to remove the systematic errors from the scan's elevation data. If the DEM creation process is repeated, we then obtain

$$E' = (e - e_1) + R \tag{4}$$

which is free of any systematic error due to the non-perpendicularity of the scanner's vertical axis with the local horizontal plane.

Because the TLS is mounted on a tripod, the distances to the targets hit by the laser beam vary. For a tripod with a limited height (1–2 m), a target located far from the scanner will be hit by a laser beam that is nearly parallel to the ground's surface. In this configuration, it will likely hit the top of objects in agricultural plots, such as crop residues or ridges, which will introduce error into the elevation scan data. Because this error is correlated with the distance (d) to the TLS position, we calculated the correlation coefficient (ρ) between E' and d. We then conducted a coefficient significance test to test the null hypothesis that $\rho = 0$ (alternative hypothesis: $\rho \neq 0$). When the null hypothesis was not accepted (i.e., E' and d were significantly correlated), the regression line

$$e_2 = a' + b' \times d \tag{5}$$

with a′ and b′ constants, was determined and used to remove this error from the elevation scan data. We then repeated the DEM creation process and obtained E'', which theoretically represents only random error.

We ascertained whether the error distribution of each DEM was normal by conducting a normality test. The random error of a DEM is generally assumed to be normally distributed (Parratt, 1961; Topping, 1962; Taylor, 1982). This assumption comes from the central limit theorem, which states that averaging a sufficiently large number of random variables yields a normal distribution (Vanmarcke, 1983; Cassela and Berger, 1990). Therefore, when a variable is considered to be the superposition of several smaller error sources, it can be assumed to be normally distributed (Heuvelink, 1998). A normal distribution has two parameters: the mean (μ) and the standard deviation (σ). In many cases, if the systematic error has been removed, it is reasonable to assume that the mean is zero (Temme et al., 2009).

We first conducted a test of equal variance to compare the error variability between the different scans. We then calculated the mean ($\mu_{E''}$) of E'' and performed a means test to test the null hypothesis. The null hypothesis test is expressed by $\mu_{E''} = 0$ (i.e., the mean random error attributable to farming activity is equal to zero; the alternative hypothesis is $\mu_{E''} \neq 0$). If the null hypothesis was rejected (i.e., the mean was significantly different from 0), the mean was added to the elevation scan data to ensure that the new mean ($\mu_{E''}$) of E''' (calculated from the newly generated DEM) was zero. Fig. 5 shows a flowchart of the method used to address the errors in the TLS point elevations.

After the systematic error had been removed and the mean error was determined to be zero, the 14 corrected scans were merged to obtain a point cloud of the watershed. The method described by Guarnieri et al. (2009) was used to generate a DEM (1 × 1 m spatial resolution) over the area of interest. The remaining holes in the DEM were then filled using the mean values of the surrounding pixels within a 5 × 5 pixel window centered on the pixel of interest. To detect and remove local outliers, we applied the method suggested by Felicisimo (1994) because some erroneous points related to the tops of the crops remained despite the use of a local minimum elevation filter. In this method, the probability of finding a certain elevation value within the neighborhood of a pixel is calculated by comparing the original elevation of a pixel with the values estimated from the neighbors:

$$\delta_i = \hat{z}_i^{NB} - z_i \tag{6}$$

where δ_i is the difference between the original and estimated values at the i-th pixel, NB is the number of neighbors, $\hat{z}_i^{NB}$ is the elevation estimated from the NB neighbors, and z_i is the original elevation.

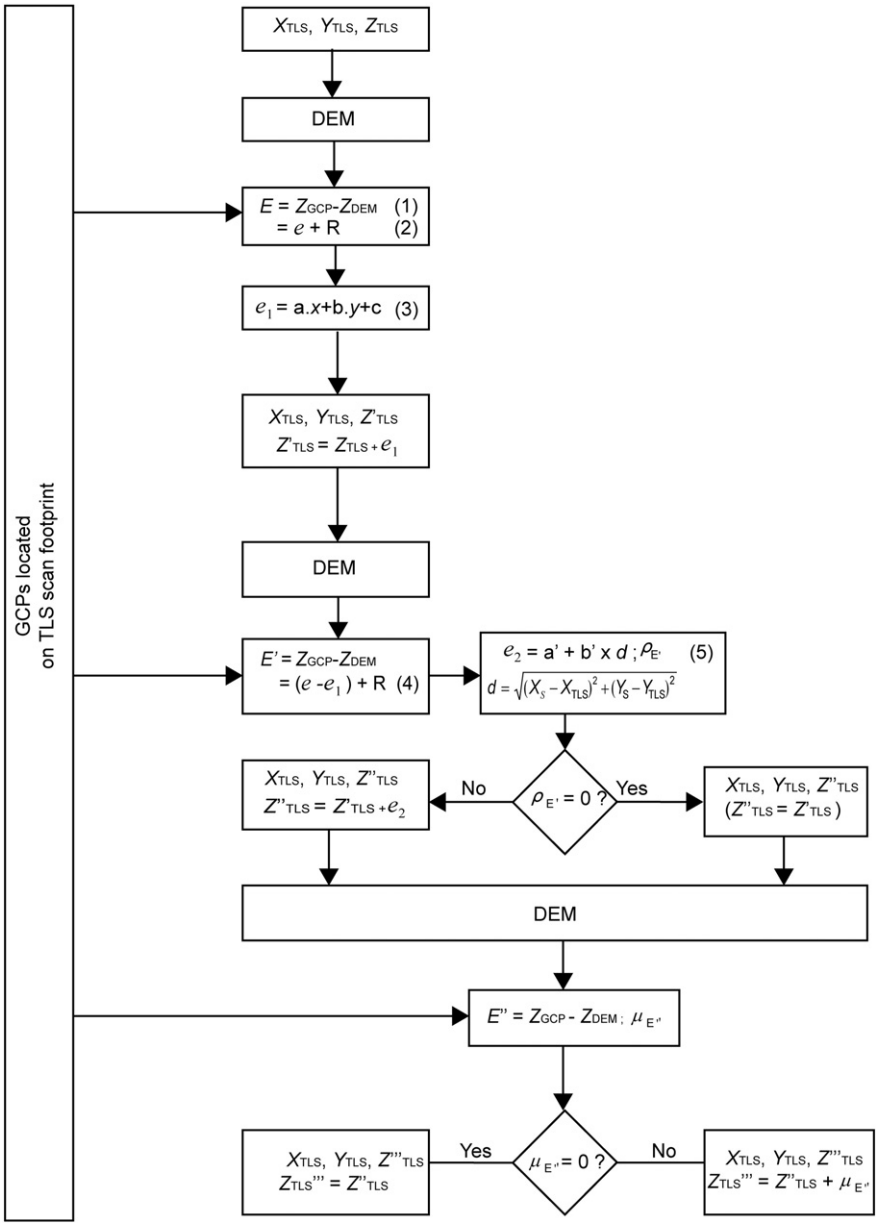

Fig. 5. Flowchart of TLS data processing for error removal.

When δ_i $(i = 1\ldots n)$ is determined for every pixel, the overall average and standard deviation (STD) ($\overline{\delta}$ and s_δ) can be calculated. Assuming a Gaussian distribution of δ_i, Student's t-test can be used to standardize the difference:

$$t_i = (\delta_i - \overline{\delta})/s_\delta \quad i = 1, \ldots, n \tag{7}$$

where n is the total number of pixels. An outlier is detected when $|t_i| \geq t_{\alpha/2,\infty}$, and the original erroneous value z_i is then replaced by $\hat{z}_i^{NB}$ for each neighboring i-th pixel. Otherwise, a new value of $\hat{z}_i^{NB}$ is calculated from the neighboring pixels where $|t_i| \geq t_{\alpha/2,\infty}$.

Given the farming activity in the agricultural watershed, most of the error in the DEM might be observable in the field. To detect only the most significant errors, we set the value of α (significance level) to be as low as possible. This value corresponded to 0.001 in the Student's t table, leading to a $t_{\alpha/2,\infty}$ value of 3.291 for a two-tailed test. Using a computation process, the neighbors of i-th pixel were selected within a moving window centered on i. Commonly used window sizes are 3×3 and 5×5 pixels. Often, $\hat{z}_i^{NB}$ is calculated as either the mean of the neighboring pixel values or as a kriged value. Felicisimo (1994) found that the mean method was simple and sufficient for obtaining an adequate substitution value. In this study, we calculated $\hat{z}_i^{NB}$ as the mean of the neighboring pixels located in a 5×5 window. When a pixel value was detected as an outlier, one or more surrounding pixel values were generally also erroneous. Using a window size of 3×3 in such a case could thereby limit the number of pixel values from which the new, replaced value of $\hat{z}_i^{NB}$ is calculated.

2.3.2. UAS photogrammetry

Approximately 760 aerial images were acquired in a single flight, and a manual interrogation check confirmed that all the images were sharp (i.e., not blurred or over- or under-exposed) and could be used for 3D restitution. For image-based surface reconstruction, we used a similar workflow based on two software packages: the recently launched (commercial) computer vision Agisoft PhotoScan software v0.84 (http://www.agisoft.ru) and the open-source toolbox for experimental photogrammetry, MicMac (http://www.micmac.ign.fr/), which was developed by the National Geographic Institute of France (NGIF).

The Agisoft PhotoScan software was reviewed by Verhoeven (2011), while MicMac was reviewed by Pierrot Deseilligny and Clery (2011).

Three-dimensional restitution from multi-view imagery is a complex process that requires several steps. The workflow used in this study is outlined in Table 2, where the differences between the two software packages are apparent. Initially, the camera was calibrated to take lens distortion into account. Feature points (e.g., corners or characteristic points) were then extracted from each image using a scale invariant feature transform (SIFT) algorithm (Lowe, 2004). Common feature points (tie points) were then determined for each overlapping image pair and used to compute a relative orientation of the block at low altitude (automatic aerial triangulation by means of bundle adjustment). The image block was then georeferenced using the GCPs (*RMSE* of 0.05 m). Subsequently, a DEM was generated using dense matching algorithms. Prior to 3D restitution, the resolution of the aerial images was reduced to 1:2, leading to a resolution of 6.6 cm GSD for the DEMs produced from each software package. To generate DEMs of 1 × 1 m resolution, the original DEMs were first converted to a point layer using ArcGIS v10 and setting each grid cell value to the mean elevation of the points within the grid cell.

2.3.3. DEM accuracy assessment and comparison

DEMs obtained from the TLS data and UAS were compared with the GCPs, which were considered to be references. We calculated several common parameters to compare DEM accuracy, including *RMSE*, mean error (*ME*), *STD* and mean absolute error (*MAE*). Elevations along a transect were analyzed to determine whether variations in the topography of the agricultural watershed were readily discernible in the UAS photogrammetry and TLS data. A DEM (1 × 1 m resolution) generated from the GCPs by applying ordinary kriging was used as a reference because it was derived from coarse resolution data and produced a very smooth DEM.

3. Results

3.1. TLS data

Due to farming activities, the TLS points were collected individually without linked targets that could be co-registered to ensure continuity between scans. Coveney and Fotheringham (2011) showed, however, that the co-registration process is not perfect and leads to error of up to 4 cm. In this study, the scan data were analyzed individually to remove systematic errors that could affect data meshing. Table 3 (columns 4 to 6) summarizes the errors that were calculated from the 14 DEMs generated directly from the original TLS elevation points; these elevations were estimated using TLS and were not changed. As the table shows, the number of GCPs differs; scan stations near the center of the watershed had more GCPs. This was expected because the GCPs were limited to the delineated watershed. The mean errors ranged from −15.5 to 4.8 cm, where negative values imply that the DEM elevations were overestimated and positive values denote underestimation. The negative mean errors were within the range of the errors obtained in many other studies (Guarnieri et al., 2009; Coveney et al., 2010). The positive means, however, were new and were associated with stations located on a plot after the sugar beet harvest (Soil C). This soil structure remained after the harvesting of sugar beets and the soil had been compacted by harvesting vehicles. Many studies have highlighted soil displacement by heavy vehicles during sugar beet harvesting operations (Arvidsson et al., 2000; Trautner and Arvidsson, 2003); therefore, the positive mean errors could have been caused by the soil being compacted by tractor wheels.

These TLS points were therefore underestimated compared with a situation where the soil surface had been plowed or contained some crop residues. The GCP elevations were also collected when the plots were plowed. Plowing preserves nutrients from weeds and previous crops by burying them in the upper layer of the soil; it also aerates the soil and provides good conditions for seeding alternate crops. This operation leads to an upward displacement of the topsoil, resulting in an overestimation of the GCP elevations.

The errors from stations on a soil that was tilled using a moldboard plow (Soil A) had the highest absolute mean errors. Field measurements on this soil were difficult because the soil was loose as a result of plowing. It was difficult to ensure the stability of the tripod when the TLS was rotating. In addition, the tripod height measurements may have contained errors. Given the soil roughness caused by plowing, it was difficult to obtain a topsoil reference from which the tripod height could be measured. In addition to these errors, the overestimation of TLS point elevations on Soil A was also due to the vertical displacement of the soil by plowing. These conditions did not occur on a soil that was tilled using a disk harrow after the wheat harvest (Soil B), which was smoother and provided better stability for the tripod and a more precise measurement of the tripod height. The presence of wheat or grass, however, tended to significantly overestimate the point elevations because the laser beam would hit the crops rather than the soil surface.

Table 3 shows the values of *ME*, *RMSE* and *STD* that were calculated from the DEMs generated after removing the errors associated with the *x* and *y* coordinates from the scan data. *MAE* and *RMSE* therefore decreased given that most of the errors were spatially correlated with *x* and *y*. The results are more impressive for stations on Soil A. The method reduced *RMSE* from initial values of 11.7 to 17.7 cm to only 3.0 to 6.4 cm. Irrespective of soil tillage, the mean errors ranged from −1.5 to 4.8 cm, and the *RMSE* ranged from 3.0 to 8.5 cm. In contrast, this treatment had no significant effect on the *STD* values, which remained nearly unchanged. These results were expected because, theoretically, the variance of $Z_{GCP} - Z_{DEM}$ is equal to the variance of $Z_{GCP} - Z_{DEM} \pm f(x, y)$.

Table 2
Workflow showing the image processing steps using the PhotoScan Agisoft and MicMac software packages.

Process	Description	PhotoScan		MicMac toolbox	
		Tool name	Specificity	Tool name	Specificity
Camera calibration	Modeling of the inner geometry (interior orientation) of the camera	Agisoft Lens	With a set of checkerboard images	Apero	With a set of convergent images of a 3D objet
Feature point extraction	Extraction of point of interest for each image	Align tool	Similar approach than SIFT	Tapioca	SIFT algorithm
Tie point generation	Determining common feature points on image pairs				
Image orientation	Computing simultaneously the poses of each camera and the position of tie points in a relative system (aerotriangulation by means of bundle block adjustment)			Apero	Offers much fine control parameterization
Georeferencing	Transform the relative orientation in absolute orientation	Optimize tool		Bascule	
Surface reconstruction by dense matching	Multi-view geometry restitution by ray intersection	Building geometry	Triangulate the dense cloud points to produce a mesh and then simplify this mesh	MicMac	Multiscale pixel-based matching approach: surface reconstruction is performed from coarse to fine resolution.

Table 3
ME, *RMSE* and *STD* calculated from DEMs generated using original TLS scan point elevations, TLS scan point elevations after removing errors correlated with *x* and *y* coordinates, and TLS scan point elevations after removing errors correlated with the distance to the scanner position.

Stations	Soil tillage	Number of GCPs	From original TLS scans			After removing errors correlated with *x* and *y* coordinates (1)			After removing (1) and errors correlated with distance to scanner position		
			Mean (cm)	*RMSE* (cm)	*STD* (cm)	Mean (cm)	*RMSE* (cm)	*STD* (cm)	Mean (cm)	*RMSE* (cm)	*STD* (cm)
ST1	A	301	−15.5	16.3	5.1	−4.5	6.4	4.5	0.0	4.0	4.0
ST2	A	228	−16.9	17.7	5.3	0.6	4.5	4.4	0.0	4.4	4.4
ST3	A	194	−11.3	12.2	4.6	−0.7	4.5	4.5	0.0	4.3	4.4
ST4	A	181	−14.5	15.1	4.2	0.0	3.9	3.9	0.0	3.9	4.0
ST5	A	179	−11.0	11.7	4.1	−1.2	3.8	3.6	−1.0	3.8	3.7
ST6	C	137	1.8	3.7	3.2	0.0	3.0	3.1	0.0	3.0	3.0
ST7	C	136	2.9	4.4	3.3	−1.5	3.6	3.2	−1.0	3.6	3.2
ST8	C	154	4.8	6.4	4.4	0.8	4.0	3.9	0.0	3.9	3.9
ST9	B	100	−6.1	10.0	7.9	4.8	8.5	7.0	0.0	6.2	6.2
ST10	B	57	−8.8	10.3	5.5	−2.8	5.5	4.9	0.0	4.6	4.6
ST11	B	73	−3.0	5.7	4.9	0.9	4.5	4.5	0.9	4.5	4.5
ST12	B	51	−4.8	6.2	3.9	1.3	3.9	3.7	0.0	3.4	3.4
ST13	B	64	−4.5	7.7	6.6	0.0	6.5	6.6	0.6	4.5	4.5
ST14	B	232	−0.1	4.6	4.5	0.0	4.1	4.1	0.0	3.9	4.0

Table 3 shows the *ME*, *RMSE* and *STD* of the DEM error after removing errors that were correlated with distance to the scanner position. The mean errors ranged from −1 to 0.9 cm, which is close to 0. Irrespective of soil tillage, only four stations out of 14 had mean errors that were not null. It is worth noting how close the obtained *RMSE* values were to the *STD* values. The systematic error removal methods appear to be optimal. *RMSE* and the estimated variances were calculated with the method of Deakin and Kildea (1999):

$$(RMSE)^2 = \sigma^2 + (estimate\ \ of\ \ bias)^2 \quad (8)$$

which means that if the bias was removed, *RMSE* and variance should be equal. Conformity tests of the variance to the square of *RMSE* showed that all the variances were equal to their corresponding *RMSE* at a significance level of $\alpha = 0.05$. We can thus conclude that all the biases were successfully removed from the errors computed in the TLS data.

Fig. 6 shows the histograms of the errors obtained after removing the errors that were correlated with the distance to the scanner position. A normality test performed at a significance level of $\alpha = 0.001$ on the errors showed that only the distribution of errors from ST3 could not be considered to be normal. However, given that its histogram could be approximated by a bell-shaped distribution, we assumed that it was normal for the remainder of the analysis.

A test of equal variances at a significance level of $\alpha = 0.001$ (null hypothesis is H_0: $\sigma^2_{ST_1} = \ldots = \sigma^2_{ST_n}$; alternative hypothesis is H_a: $\sigma^2_{ST_1} \neq \ldots \neq \sigma^2_{ST_n}$) performed on the scan data showed that the variances were significantly different. Despite the lack of variance homogeneity, we tested the equality of the mean errors. The mean errors, which ranged from −1 to 0.9 cm, were found to be significantly different given that the equal means test rejected the null hypothesis.

The means were also significantly different. This was confirmed by a means test to determine zero for stations ST5, ST7, ST11 and ST13, where the null hypotheses were all rejected. Non-zero mean errors denote errors that were not correlated with *x* and *y* or with the distance to the scanner position. Only a few stations on the same soil type had mean errors that were not zero. This was the case for stations ST5 on Soil A, ST7 on Soil C, and ST11 and ST13 on Soil B and was likely due to the soil structure, which was not identical from one station to another within the same soil tillage type.

Table 4 shows the calculated parameters after removing the mean errors from the scan data. This process involved only the data from stations ST5, ST7, ST11 and ST13. The values of the errors in Table 4 are identical to the errors remaining after removing the errors that were correlated with the distance to the scanner position, other than the means of stations ST5, ST7, ST11 and ST13, which were previously set to zero. The mean removal process had no impact on the final *RMSE* because these mean values were very small.

Fig. 7 shows the decrease in *RMSE* as we applied the systematic error removal methods. The final *RMSE* values differed from zero, which indicated differences between the TLS data and the GCPs. Apart from stations ST9 and ST13, the error correlated with *x* and *y* was high and was the largest for the stations on Soil A. On this soil, the error that was correlated with the distance to the scanner position was insignificant (compared with the error that was correlated with *x* and *y*), which differed from stations ST1, where the soil was free of crops or crop residues. This result could be explained by the fact that the ST1 footprint radius was high compared with those of ST2, ST3, ST4 and ST5.

Plowed soils are characterized by successive ridges, which give them a sinusoidal pattern (Fig. 8). Therefore, the area between two successive ridges has a lower elevation that can be obscured by objects in the foreground (i.e., the ridges). Wolf and Dewitt (2000) described these regions as "dead ground". The greater the distance to the scan, the more likely it is that the laser beam will hit the ridge tops, which introduce errors in the TLS point elevation estimations.

Only the errors that were correlated with *x* and *y* were present at the stations on Soil B. This result was expected because the plots were completely free of crops or crop residues that could interrupt the laser beam. In addition, the plot soils had been compacted by sugar beet harvesting vehicles before the collection of the TLS data, leaving the soil surface flat and free of any patterns, such as ridges, that could intercept the laser beam.

Other than ST11, the stations on Soil C presented errors that were correlated with *x* and *y* and with the distance to the TLS position, but these errors were less important than those from the stations on Soil A. Although this soil was tilled, its surface was less patterned. The data collection conditions were more optimal than those on Soil A. The soil surface was less rough, and it was not ridged. The error that was correlated with the distance to the scanner was mainly caused by the presence of crops and crop residues. The decrease in *RMSE* values differed from one station to another, which could be explained by the fact that the plants at each station differed in height, although they were all less than 10 cm.

3.2. Comparison of the DEMs

The DEMs generated from the merged TLS scan data (after they had been processed to remove the systematic errors and non-zero means) and the UAS photogrammetry data were compared with the GCP elevations (Fig. 9). Only a few of the absolute errors from DEM_{TLS} (DEM generated from the TLS data; Fig. 9A) were greater than 15.1 cm.

Approximately 96% of the absolute errors were less than 10 cm, and 99% were less than 15 cm.

For DEM_{PSC} (DEM generated from the UAS data using Agisoft PhotoScan; Fig. 9B), 57% of the absolute errors were less than 10 cm, and 72% were less than 15 cm. The absolute errors greater than 15.1 cm were systematically located near the watershed boundary. The 3D model created with the Agisoft PhotoScan software had a non-linear (parabolic) distortion that overestimated the terrain elevation on the image block border. Although the accuracy of the elevation of the image block center was good, the systematic overvaluation of the terrain increased as the distance from the center increased. This shift has been referred to as the 'bowl effect' by some users of Agisoft PhotoScan (e.g., on the Agisoft PhotoScan forum: http://www.agisoft.ru/forum/).

As mentioned by Yuan (2009), the reasons for this reduced accuracy on the block border are that the photogrammetric points on the periphery are seen on fewer images and that the intersection angles are relatively small. Therefore, fewer image rays are used to compute the position of the peripheral points, and the intersection angles are lower than the points at the center of the block. In contrast, the DEMs generated with MicMac (DEM_{MCM}, Fig. 9C) do not show a parabolic distortion.

Table 4
ME, *RMSE* and *STD* calculated for each scan after removing the mean errors from ST5, ST7, ST11 and ST13 point elevations.

Stations	Soil tillage	Mean (cm)	*RMSE* (cm)	*STD* (cm)
ST1	A	0	4.0	4.0
ST2	A		4.4	4.4
ST3	A		4.3	4.4
ST4	A		3.9	4.0
ST5	A		3.8	3.7
ST6	C		3.0	3.0
ST7	C		3.6	3.2
ST8	C		3.9	3.9
ST9	B		6.2	6.2
ST10	B		4.6	4.6
ST11	B		4.5	4.5
ST12	B		3.4	3.4
ST13	B		4.5	4.5
ST14	B		3.9	4.0

In our opinion, this difference results from the camera calibration model; MicMac provides a more precise correction (Brown's distortion model with five coefficients of radial distortion) than Agisoft PhotoScan

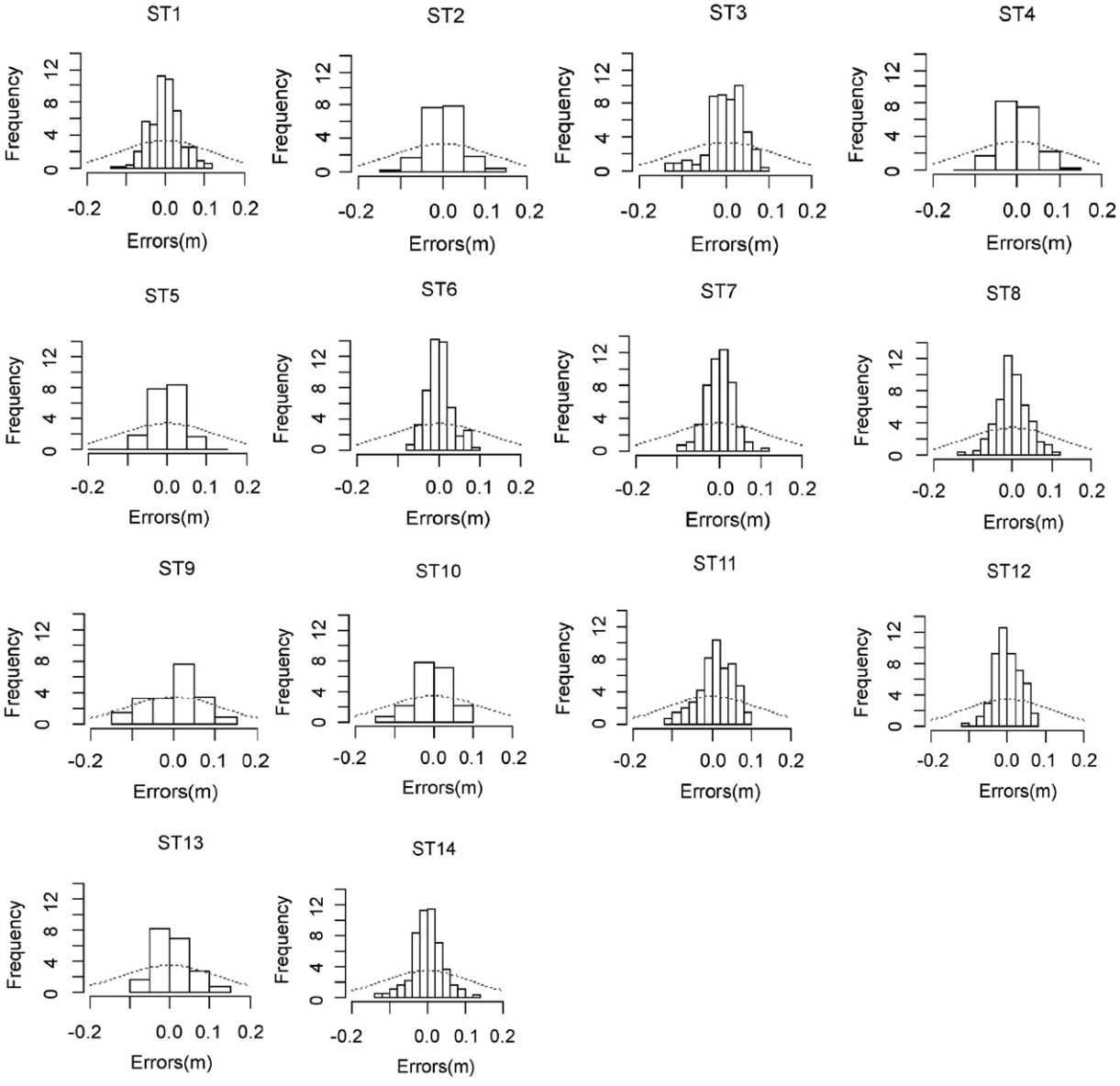

Fig. 6. Histograms of random errors from TLS scans. Dashed lines denote normal distributions computed using mean and the standard deviation.

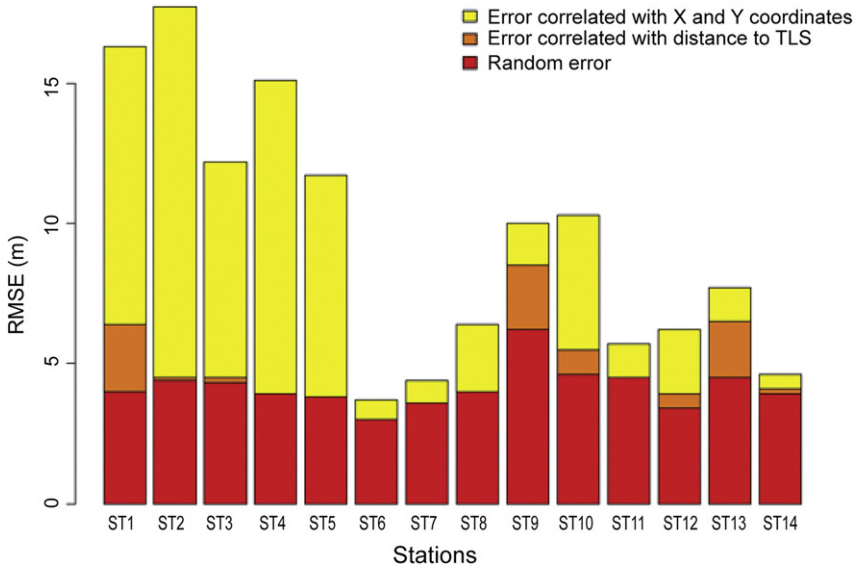

Fig. 7. *RMSE* values when applying methods for removing errors correlated with *x* and *y* coordinates and distance to TLS position.

(Brown's distortion model with three coefficients of radial distortion). Image lens distortion modeling has an important impact on the 3D restitution accuracy, and the Agisoft Lens toolbox does not appear to provide a satisfactory result in terms of camera calibration.

For DEM_{MCM}, 71% of absolute errors were less than 10 cm, and 90% were less than 15 cm. Other than the plot that was occupied by a mustard crop, most of the absolute errors greater than 10 cm were at low elevations. Although the multi-view stereo restitution accuracy depends on many interactive factors, such as image quality, surface complexity, the algorithm used and its parameterization (Egels and Kasser, 2001), the base-to-height ratio is a good indicator of the expected altimetry accuracy. 'Base' is the distance between two adjacent images, and 'height' is the flight height (i.e., the distance between the camera and the ground). The base-to-height ratio indicates the convergence of the imagery's optical rays and thus, implicitly, the accuracy of the parallax measurement (Konecny, 2002). In the study area, the difference between the maximum and minimum elevations was ±10 m, which is significant.

The small UAS flew at a constant altitude of 100 m above ground level from its takeoff location, and the flight height changed as the relief changed. The base-to-height ratio changed from 0.30 on the upper side of the watershed to 0.25 on the lower side. As shown in Fig. 9C, most of the absolute errors in the area occupied by the mustard crop (Fig. 9D) ranged from 0.15 to 0.35 cm. The DEM in this area was more of a digital surface model (DSM) than a DEM. The differences between DEM_{GPS} and DEM_{MCM} showed that the crops were high in this area. These differences varied between −5 and −35 cm and had a mean of −18 cm, which confirm that the elevations measured in this area corresponded to the tops of the mustard crop. As observed in the field, this height varied from ±10 to ±20 cm. However, the crops were not uniformly distributed on the plot; this explains why some of the differences between DEM_{GPS} and DEM_{MCM} were less than 10 cm.

Table 5 presents some of the statistics related to the DEM errors. As expected from Fig. 9, the DEM_{TLS} is the most accurate of the three models, with an *RMSE* value of 4.9 cm and an *ME* value of 0.6 cm. The very small *ME* value indicates that all the systematic errors had been removed during TLS data processing. The DEM_{PSC} has a greater *RMSE* value of 13.9 cm, which is nearly five times greater than that of the DEM_{TLS}, which has an *ME* value of −9.6 cm. A negative or non-zero mean indicates that systematic error was present and that the elevation was generally overestimated by the DEM_{PSC}. This conclusion can also be made for the DEM_{MCM}. The DEMs from the UAS data have a larger range of errors, with maximum absolute values of 52 cm for the DEM_{PSC} and 35 cm for the DEM_{CMC}.

Fig. 10 shows the spatial distribution of the elevation differences between DEM_{TLS} and DEM_{MCM} (Fig. 10A), DEM_{TLS} and DEM_{PSC} (Fig. 10B),

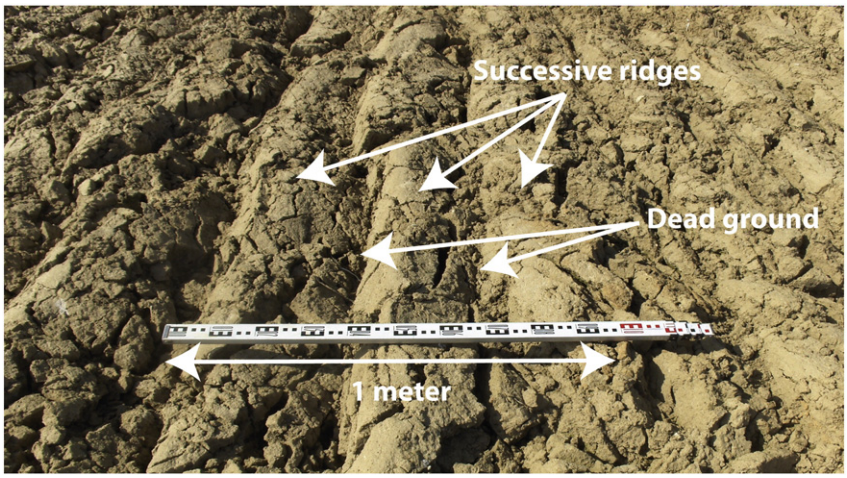

Fig. 8. Illustration of plowed soil's sinusoidal pattern due to the succession of ridges and furrows.

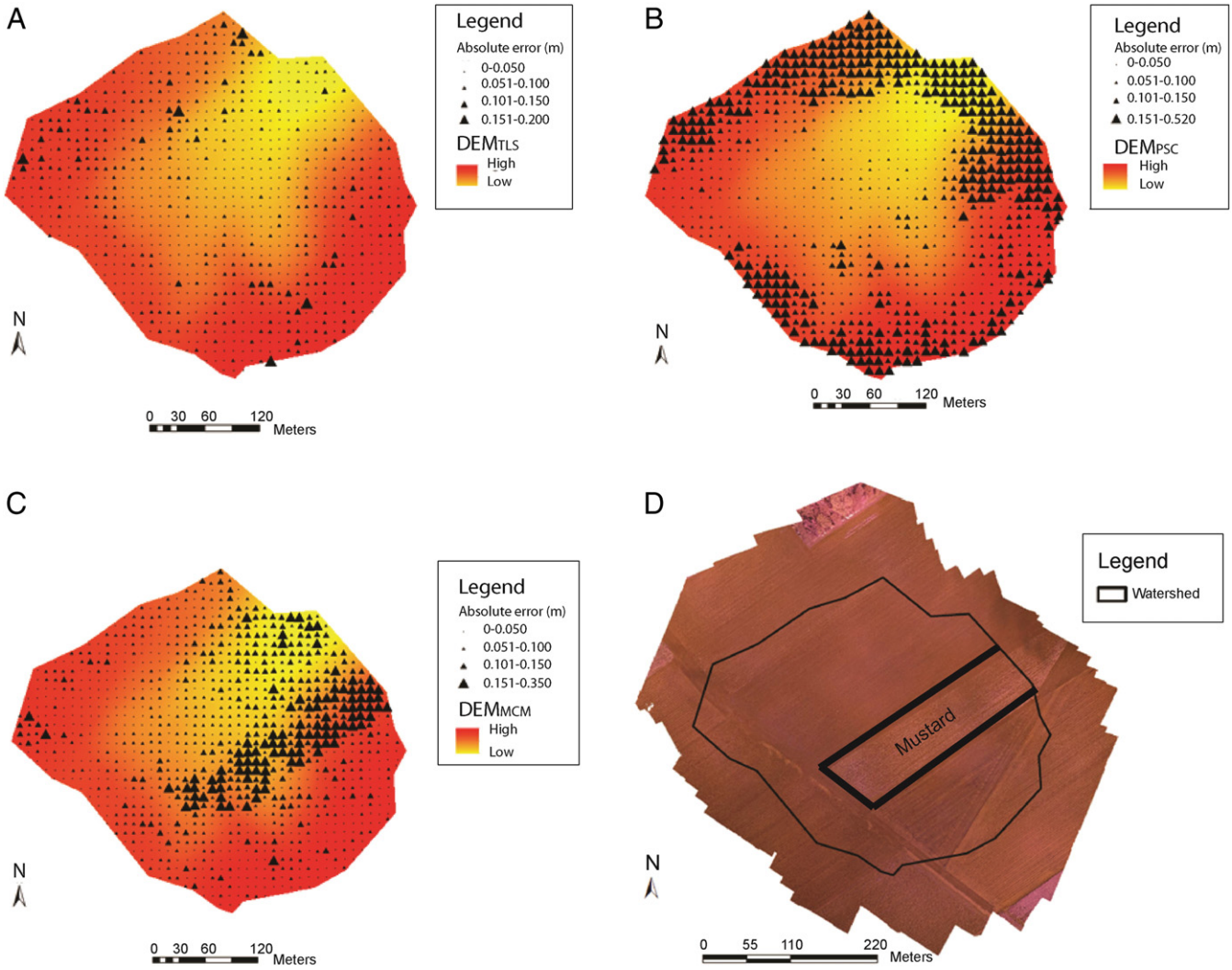

Fig. 9. Absolute errors calculated from DEMs. (A) Errors from a DEM generated from TLS data. (B) Errors generated from UAS data using Agisoft PhotoScan software. (C) Errors generated from UAS data using MicMac software. (D) Location of area cultivated with a mustard crop during UAS aerial photograph collection.

and DEM_{MCM} and DEM_{PSC} (Fig. 10C). Relative to the DEM_{TLS}, the DEM_{PSC} overestimates the elevations on the border of the watershed, with elevation differences that reach −59 cm. In contrast, the elevation differences in the center of the watershed are generally less than −7 cm. This result is specific to the DEM_{PSC} because the elevation differences of the DEM_{MCM} relative to the DEM_{TLS} are generally less than −13 cm except in the area occupied by the mustard crop, where the DEM_{MCM} elevations are higher. The DEM_{MCM} appears to overestimate the elevations in the center of the watershed relative to the DEM_{PSC}, with elevation differences of up to 30 cm.

Fig. 11 compares the elevations of the DEMs generated from the TLS and UAS data and the elevations of DEMs generated using GCPs (DEM_{GCP}) along a transect. The transect (Fig. 11D) was selected so that it crossed areas where the DEM_{MCM} and DEM_{PSC} showed high absolute errors. Although the DEM_{GPS} profile is very smooth, the high-resolution DEMs (from TLS and UAS data) had rough profiles, highlighting their ability to show the farming activities that modify the microtopography of the plot (Fig. 12). Although the DEMs generated with both technologies (TLS and UAS) are able to reveal soil microtopography, the DEM_{MCM} (Fig. 12A) better reconstructs the individual ridges and furrows, whereas the DEM_{TLS} (Fig. 12B) shows a succession of mounds and depressions.

The transect from the DEM_{TLS} better fits the topography (Fig. 11B). Although the transect crosses many of the stations, there are no discontinuities from one station to another. In contrast, the elevations were overestimated by the DEM_{PSC} along the first and last 100 m of the transect (Fig. 11A), which correspond to the borders of the watershed. The differences decreased as the distance to the transect boundaries increased. The maximum differences were 20 cm at ±15 m and 37 cm at ±340 m. The presence of mustard was not indicated in the results obtained from the DEM_{PSC}. In contrast, the DEM_{MCM} transect closely matched the profile from the DEM_{GCP} at ±130 m. The mean error at this location was −5.8 cm, which is very small. From ±130 to ±230 m, the transect was located in the area occupied by mustard. The DEM_{MCM} showed a clear difference from the DEM_{GCP} in this region; it overestimated the elevations, with a maximum difference of −30 cm and a mean difference of −18 cm.

Table 5
Basic statistical parameters calculated from DEM errors.

	DEM_{TLS}	DEM_{PSC}	DEM_{MCM}
DEM resolution (cm)	100		
Minimum (cm)	−18.0	−52.0	−37.0
Maximum (cm)	16.0	10.0	33.0
Absolute mean (cm)	3.7	10.0	7.4
STD (cm)	3.0	9.0	5.5
Mean error (cm)	0.6	−9.6	−6.8
RMSE (cm)	4.9	13.9	9.0

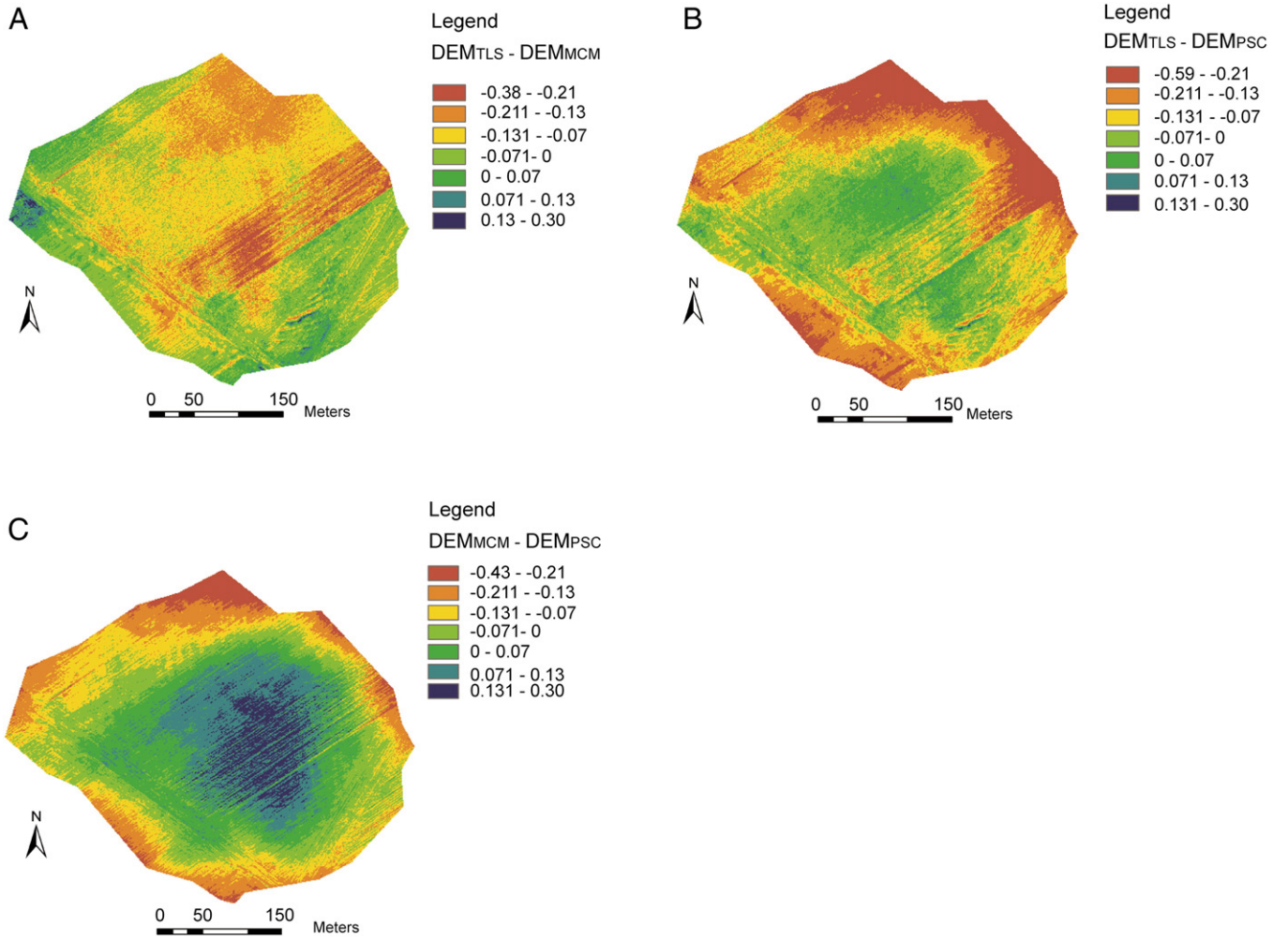

Fig. 10. Spatial distribution of elevation differences between DEMs. (A) Elevation differences between DEM_{TLS} and DEM_{MCM}. (B) Elevation differences between DEM_{TLS} and DEM_{PSC}. (C) Elevation differences between DEM_{MCM} and DEM_{PSC}.

The elevations appeared to be more variable when crops were present. From ±230 m, the difference between DEM_{MCM} and DEM_{GCP} appeared to be constant, with a mean value of −14 cm, which is, in absolute terms, 8.2 cm greater than the mean value calculated for the first ±130 m, although the soil surface was precisely the same. These portions of the transect were located on harvested plots, where the soil surface was free of crops and crop residues. The difference of 8.2 cm was most likely due to a decrease in the base-to-height ratio. Future investigations should assess the correlation between flight height and error to quantify the increase in error at low elevations. This could be helpful when choosing an optimal flight height that would minimize the error in the low elevation areas of a watershed.

4. Discussion

According to Schiewe (2000), TLS- and UAS-derived DEMs can be rated highly because their *RMSE* values do not exceed 10 cm. This study is not the first to note the high precision of these technologies. In the past five years, TLS data have been used in many studies as the data source for DEM generation. Despite the presence of obstacles, such as vegetation, the *RMSE* values of DEMs produced from TLS data can be reduced to only a few cm by filtering the data and using statistical processing techniques. Guarnieri et al. (2009) used TLS data to produce a DEM of a tidal marsh that was covered by low and dense vegetation approximately 0.3–1.0 m high. Their results showed that despite the vegetation, a DEM could be produced with a resolution of 1 × 1 m, a mean error of approximately −2 cm and an *RMSE* value of 3 cm in sparse vegetation. These values are similar to the results presented in this study (*RMSE* = 4.9 cm, *ME* = 0.6 cm). Therefore, it may be useful to consider TLS data as external validation data for quantifying the magnitude and spatial distribution of errors for DEMs of medium and low resolution DEMs (Coveney et al., 2010).

Most of the studies that have collected TLS data for DEM generation used HDS targets to co-register the scans. According to Coveney and Fotheringham (2011), co-registration errors can be up to 4 cm, which is significant in high-resolution DEMs. Nevertheless, the use of HDS targets on agricultural watersheds remains difficult because of the spatial organization of the parcels; adjacent parcels may belong to different farmers, who could have different crop tillage plans. Therefore, the scans must be surveyed individually. This study introduced a new approach for removing errors caused by not using HDS targets on agricultural watersheds by applying linear regression on the elevation errors. The collection and analysis of the TLS data, however, were time-consuming because GCPs were used on the entire watershed for the statistical analysis to allow for scan meshing. Nevertheless, given the linear behavior of the errors, a decrease in the number of GCPs could lead to similar linear relationships. Further analysis will reveal the optimum number of GCPs.

A comparison of the DEM_{PSC} with the GCPs showed that the errors tended to increase on the watershed border due to the camera calibration model; this error was referred to as the 'bowl effect'. According to Fonstad et al. (2013), the presence of such non-linear distortions in

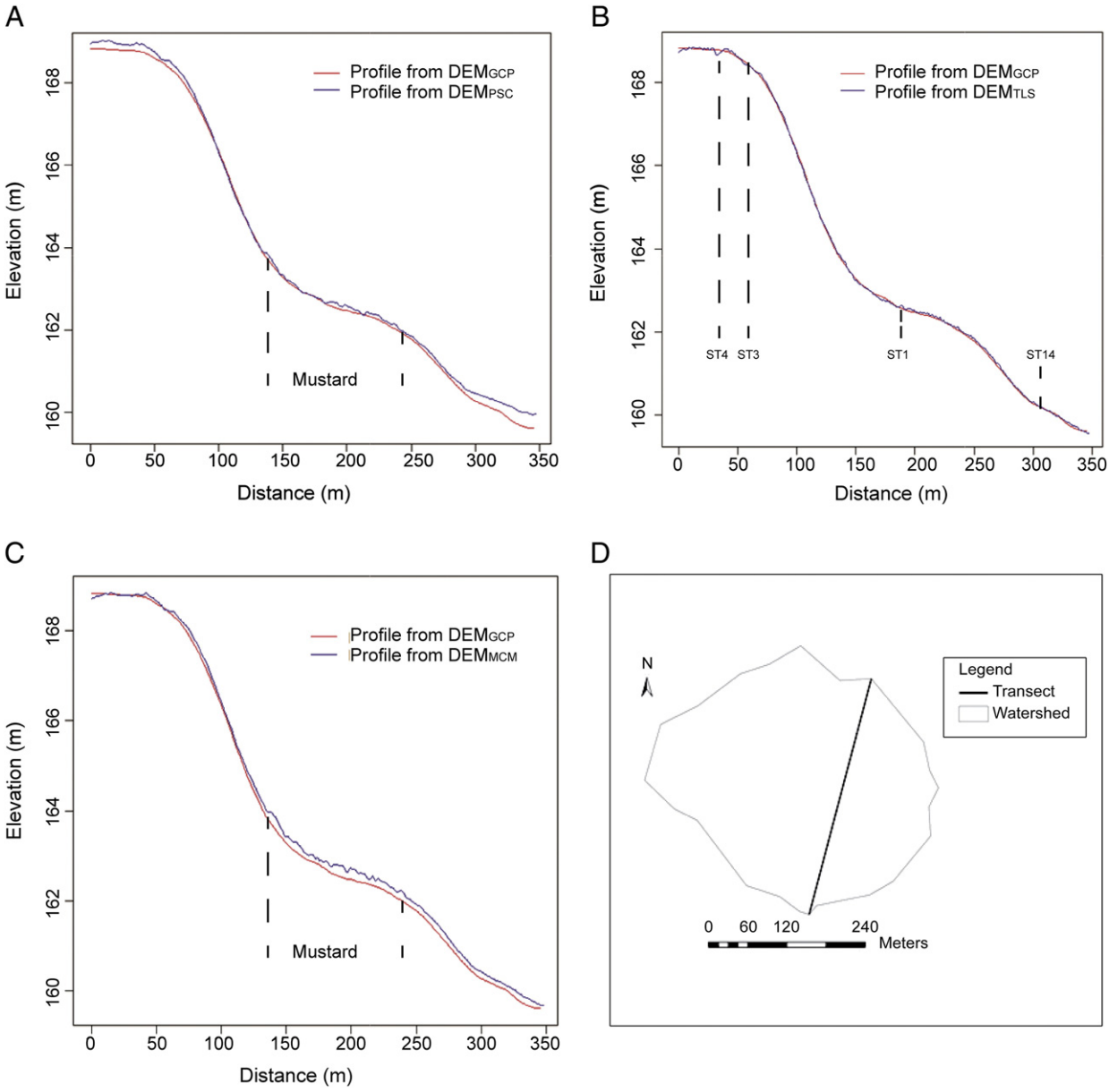

Fig. 11. Elevation evolution along a transect. (A) Profiles from DEM_{GCP} and DEM_{PSC}. (B) Profiles from DEM_{GCP} and DEM_{PSC}. (C) Profiles from DEM_{GCP} and DEM_{MCM}. (D) Location of the transect.

the DEM can severely limit the potential accuracy of structure-from-motion photogrammetry. However, using Brown's distortion model in the MicMac software package, which used five coefficients of radial distortion, we showed that the bowl effect could be largely removed. Therefore, the MicMac package shows great promise for the development of structure-from-motion photogrammetry.

We could have removed the systematic error (i.e., the 'bowl effect') by applying a regression to the differences in elevation between DEM_{PSC} and GCPs. However, unlike the DEM_{TLS}, this error is specific to the camera calibration model in the Agisoft PhotoScan software and is not due to the field conditions (e.g., crops, ridges, and soil structure). In contrast to scanner, the UAS was not in contact with the soil, and the DEM_{PSC} became a complete end product after using the structure-from-motion approach. Moreover, except for a few software packages (e.g., MicMac), the entire process is a black box to the user. Thus, the identification of systematic and random errors caused by agricultural activities, as we performed with the TLS data, remains difficult to handle.

Data collection was easier with the UAS than with the TLS because it only involved placing 10 GCPs in the field, surveying them with RTK GPS, and launching the data collector. The entire flight was autonomous. The main problem, however, is found in the data processing. The results showed that the use of two software packages could lead to different results. The DEMs generated using the MicMac software appeared to be the most accurate (with an *RMSE* value of 9 cm vs. 13.9 cm for the DEM generated using Agisoft PhotoScan) and allowed the bare plot and the plot occupied by the mustard crop to be identified. This comparison highlighted the importance of the choice of the UAS data processing tool (i.e., the implemented method).

These results confirmed the conclusion of Vallet et al. (2011), who compared DEMs extracted from UAS data with GCPs surveyed by GPS.

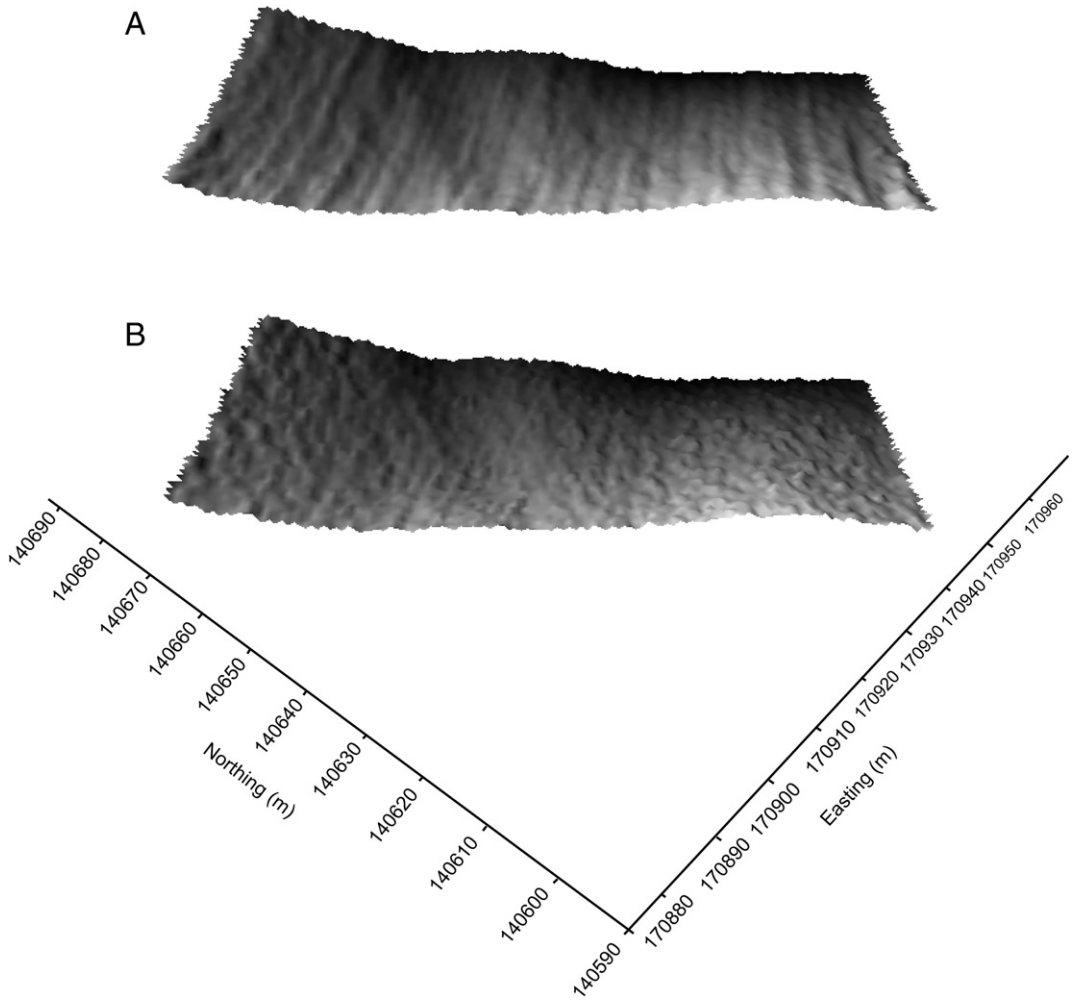

Fig. 12. Magnified images of DEMs showing the detail of a soil microtopography reconstruction. (A) DEM_{TLS}. (B) DEM_{MCM}.

These authors used two commercial software packages to process the images and extracted the DEMs: Pix4D (http://www.pix4d.com) and NGATE (http://www.socetgxp.com). Their results revealed significant differences between the software packages. For instance, Pix4D provided a mean elevation difference of 4.7 cm and an *STD* value of 9.5 cm, whereas the NGATE results were 11 cm and 26.7 cm, respectively. Nevertheless, the low *RMSE* values obtained with DEMs generated from UAS data in different applications showed that UAS is a promising technology for data acquisition on agricultural watersheds.

Nevertheless, TLS and UAS photogrammetry are not comparable in terms of affordability. The UAS Gatewing X100 technology currently costs approximately 50,000 euros (educational price), including materials and training. The body, which is made of carbon reinforced EPP (Engineered Polymer Product), costs 2500 euros and must be replaced after 50 flights. In contrast, a terrestrial laser scanner can cost two to three times the price of the UAS Gatewing X100. However, we rented the equipment from a private company for 1150 euros (including taxes) per day of surveying. There is no way that UAS photogrammetry is more affordable, even though some UAS systems can cost much less, depending on their complexity.

The ability of UAS data to highlight crop height variability could be helpful for analyzing crop growth and could be used as supplementary data for crop growth models. Many studies have used crop growth models for applications that range from analyzing yield potential and improving pesticide, nutrient and water management to estimating aboveground dry biomass (Liu et al., 2010; Palosuo et al., 2011; Claverie et al., 2012; Rötter et al., 2012).

Both TLS and UAS photogrammetry represent promising opportunities for collecting high density, fine-resolution topographic data while taking account of microtopographic variability. This is especially apparent in agricultural watersheds where their role in quantifying soil surface depression storage (Planchon et al., 2002; Abedini et al., 2006; Martin et al., 2008), estimating infiltration and runoff (Gascuel-Odoux et al., 1991; Watts and Hall, 1996; Le Bissonnais et al., 1998; Spaan et al., 2005) and calculating soil erosion and deposition (Yang et al., 2009; Gessesse et al., 2010) has been highlighted. Deriving hydrological parameters from high-resolution DEMs generated from such data could allow for the analysis of microtopography at the watershed level.

Agricultural soil microtopography causes ridges and depressions in the generated DEMs. Certain hydrological applications, such as water drainage extraction, require a DEM model that does not have depressions, and this constraint is accepted by many hydrologists as a necessary evil (Wechsler, 2007). Many algorithms have been developed to assign flow directions in depressions; depending on the strategy, depressions are either filled (Jenson and Domingue, 1988; Martz and Jong, 1988; Soille and Gratin, 1994) or carved (Martz and Jong, 1988; Morris and Heerdegen, 1988; Rieger, 1998; Martz and Garbrecht, 1999). Several studies have also used combinations of both strategies (Soille, 2004a,b; Lindsay and Creed, 2005). Many studies have compared different strategies for removing depressions in DEMs and have

shown that depression removal algorithms can impact the extracted final drainage water (Lindsay and Creed, 2005; Zhu et al., 2006; Grimaldi et al., 2007).

Moreover, removing depressions from DEMs assumes that they are artifacts, which is not the case in agricultural watersheds. Therefore, the removal of depressions remains debatable. Few studies have considered depressions as existing features of the terrain (Temme et al., 2006). The use of high-resolution DEMs generated from TLS and UAS data to extract drainages water on agricultural watersheds calls into question the need for depression removal.

5. Conclusion

Farming activities on agricultural watersheds continuously change the microtopography and make the watersheds very difficult to model. The main aims of this study were to investigate the suitability of using TLS and UAS data for generating high-resolution and accurate DEMs of agricultural watersheds and to identify the strengths and weaknesses of both technologies.

The results indicate that TLS data collection was possible on agricultural watersheds, although HDS targets were not used to mesh adjacent TLS scans. All the TLS scan data, however, had to be statistically processed individually using GCPs surveyed by RTK GPS, to remove systematic errors that were correlated with the *x* and *y* coordinates and with the distance to the scanner position. The obtained *RMSE* values showed that the linear relationships applied to remove those errors were optimal because the *RMSE* values of the errors were equal to the *STD* values. Therefore, future work should attempt to use only a few GCPs for the error analysis.

DEMs of agricultural watersheds can be generated from UAS-photogrammetry data using the Agisoft PhotoScan and MicMac software packages. However, the DEM_{PSC} showed greater errors on the watershed border (i.e., the bowl effect) due to the camera calibration model, which used Brown's distortion model with three coefficients of radial distortion rather than the five coefficient used in the model for the DEM_{MCM}.

The error assessment showed that the DEM derived from TLS data was more accurate, with an *RMSE* value of 4.5 cm, than the DEMs derived from UAS photogrammetry data (9.0 cm for the DEM_{MCM} and 13.9 cm for the DEM_{PSC}). However, the DEM_{TLS} failed to reconstruct individual ridges and furrows in the agricultural soil.

References

Abedini, M.J., Dickinson, W.T., Rudra, R.P., 2006. On depressional storages: the effect of DEM spatial resolution. J. Hydrol. 318, 138–150.

Aber, J.S., Aber, S.W., Pavri, F., 2002. Unmanned small-format aerial photography from kites for acquiring large scale, high-resolution, multiview-angle imagery. In: R.S.a.S.I.S. The International Archives of the Photogrammetry (Ed.), Percora 15, Land Satellite Information IV and ISPRS Commission I Conference, Proceedings, Denver, CO, USA.

Arvidsson, J., Trautner, A., van den Akker, J.J.H., Schjonning, P., 2000. Subsoil compaction caused by heavy sugarbeet harvesters in southern Sweden. II. Soil displacement during wheeling and model computations of compaction. Soil Tillage Res. 60, 79–89.

Barneveld, R.J., Seeger, M., Maalen-Johansen, I., 2013. Assessment of terrestrial laser scanning technology for obtaining high-resolution DEMs of soils. Earth Surf. Process. Landf. 38, 90–94.

Bogner, C., Mirzaei, M., Ruy, S., Huwe, B., 2013. Microtopography, water storage and flow patterns in a fine-textured soil under agricultural use. Hydrol. Process. 27, 1797–1806.

Brinkman, R., O'Neill, C., 2000. LiDAR and photogrammetric mapping. Mil. Eng. 605, 56–57.

Carmi, G., Berliner, P., 2008. The effect of soil crust on the generation of runoff on small plots in an arid environment. Catena 74, 37–42.

Cassela, G., Berger, R., 1990. Statistical Inference. Cengage Learning, Pacific Grove.

Cerdan, O., Souchère, V., Lecomte, V., Couturier, A., Le Bissonnais, Y., 2002. Incorporating soil surface crusting processes in an expert-based runoff model: sealing and transfer by runoff and erosion related to agricultural management. Catena 46, 189–205.

Claverie, M., Demarez, V., Duchemin, B., Hagolle, O., Ducrot, D., Marais-Sicre, C., Dejoux, J., Huc, M., Keravec, P., Béziat, P., Fieuzal, R., Ceschia, E., Dedieu, G., 2012. Maize and sunflower biomass estimation in southwest France using high spatial and temporal resolution remote sensing data. Remote Sens. Environ. 124, 844–857.

Coveney, S., Fotheringham, A.S., 2011. Terrestrial laser scan error in the presence of dense ground vegetation. Photogramm. Rec. 26, 307–324.

Coveney, S., Fotheringham, A.S., Charlton, M., McCarthy, T., 2010. Dual-scale validation of a medium-resolution coastal DEM with terrestrial LiDAR DSM and GPS. Comput. Geosci. 36, 489–499.

Deakin, R.E., Kildea, D.G., 1999. A note on standard deviation and RMS. Aust. Surv. 44, 74–79.

Egels, Y., Kasser, M., 2001. Digital Photogrammetry. Taylor & Francis, Bristol.

Ehlert, D., Heisig, M., 2013. Sources of angle-dependent errors in terrestrial laser scanner-based crop stand measurement. Comput. Electron. Agric. 93, 10–16.

Eisenbeiss, H., 2009. UAV Photogrammetry. Phd thesis ETH, Zurich (199 pp.).

Eisenbeiss, H., Zhang, L., 2006. Comparison of DSMs generated from mini UAV imagery and terrestrial laser scanner in a cultural heritage application. Int. Arch. Photogramm. Remote. Sens. Spat. Inf. Sci. XXXVI, 90–97.

Eitel, J.U.H., Vierling, L.A., Long, D.S., 2010. Simultaneous measurements of plant structure and chlorophyll content in broadleaf saplings with a terrestrial laser scanner. Remote Sens. Environ. 114, 2229–2237.

Eitel, J.U.H., Williams, C.J., Vierling, L.A., Al-Hamdan, O.Z., Pierson, F.B., 2011a. Suitability of terrestrial laser scanning for studying surface roughness effects on concentrated flow erosion processes in rangelands. Catena 87, 398–407.

Eitel, J.U.H., Vierling, L.A., Long, D.S., Hunt, E.R., 2011b. Early season remote sensing of wheat nitrogen status using a green scanning laser. Agric. For. Meteorol. 151, 1338–1345.

Fabris, M., Pesci, A., 2005. Automated DEM extraction in digital aerial photogrammetry: precision and validation for mass movement monitoring. Ann. Geophys. 48, 973–988.

Felicisimo, A.M., 1994. Parametric statistical method for error detection in digital elevation models. ISPRS J. Photogramm. Remote. Sens. 49, 29–33.

Fonstad, M.A., Dietrich, J.T., Courville, B.C., Jensen, J.L., Carbonneau, P.E., 2013. Topographic structure from motion: a new development in photogrammetric measurement. Earth Surf. Process. Landf. 38, 421–430.

Fotinopoulos, V., 2004. Balloon photogrammetry for archaeological surveys. In: R.S.a.S.I.S. International Archives of the Photogrammetry (Ed.), ISPRS Congress, Istanbul, Turkey, pp. 504–507.

Gascuel-Odoux, C., Bruneau, P., Curmi, P., 1991. Runoff generation: assessment of relevant factors by means of soil microtopography and micromorphology analysis. Soil Technol. 4, 209–219.

Gessesse, G.D., Fuchs, H., Mansberger, R., Klik, A., Rieke-Zapp, D.H., 2010. Assessment of erosion, deposition and rill development on irregular soil surfaces using close range digital photogrammetry. Photogramm. Rec. 25, 299–318.

Gonzalez-Aguilera, D., Gomez-Lahoz, J., 2009. Forensic terrestrial photogrammetry from a single image. J. Forensic Sci. 54, 1376–1387.

Gooch, M.J., Chandler, J.H., Stojic, M., 1999. Accuracy assessment of digital elevation models generated using the ERDAS Imagine OrthoMAX digital photogrammetric system. Photogramm. Rec. 16, 519–531.

Gordon, S.J., Lichti, D.D., Stewart, M.P., Franke, J., 2003. Structural deformation measurement using terrestrial laser scanners. Proceedings of 11th International FIG Symposium on Deformation Measurements, Santorini Island (Greece).

Goulette, F., 2009. Relevés laser urbains par systèmes mobiles de cartographie. Revue XYZ 119, 21–25.

Grimaldi, S., Nardi, F., Benedetto, F.D., Istanbulluoglu, E., Bras, R.L., 2007. A physically-based method for removing pits in digital elevation models. Adv. Water Resour. 30, 2151–2158.

Gruen, A., 2012. Development and status of image matching in photogrammetry. Photogramm. Rec. 27, 36–57.

Guarnieri, A., Pirotti, F., Pontin, M., Vettore, A., 2006. 3D surveying for structural analysis applications. Proceedings of 3rd IAG Symposium on Geodesy for Geotechnical and Structural Engineering/12th FIG Symposium on Deformation Measurement, Baden (Austria).

Guarnieri, A., Vettore, A., Pirotti, F., Menenti, M., Marani, M., 2009. Retrieval of small-relief marsh morphology from Terrestrial Laser Scanner, optimal spatial filtering, and laser return intensity. Geomorphology 113, 12–20.

Haala, N., Cramer, M., Weimer, F., Trittler, M., 2011. Performance test on UAV-based photogrammetric data collection. In: R.S.a.S.I.S. International Archives of the Photogrammetry (Ed.), Conference on Unmanned Aerial Vehicle in Geomatics, Zurich, Switzerland, pp. 1–6.

Hammad, A.H.A., Børresen, T., Haugen, L.E., 2006. Effects of rain characteristics and terracing on runoff and erosion under the Mediterranean. Soil Tillage Res. 87, 39–47.

Hardin, P.J., Jensen, R.R., 2011. Small-scale unmanned aerial vehicles in environmental remote sensing: challenges and opportunities. GISci. Remote Sens. 48, 99–111.

Henry, J.B., Malet, J.P., Maquaire, O., Grussenmeyer, P., 2002. The use of small-format and low-altitude aerial photos for realization of high-resolution DEMs in mountainous areas: application to the Super-Sauze earthflow (Alpes-de-Haute-Provence, France). Earth Surf. Process. Landf. 27, 1339–1350.

Herbin, T., 2012. Nivellement par balayage laser. Revue XYZ 132, 41–46.

Heuvelink, G.B.M., 1998. Error Propagation in Environmental Modeling with GIS. Taylor & Francis, London.

Hirano, A., Welch, R., Lang, H., 2003. Mapping from ASTER stereo image data: DEM validation and accuracy assessment. ISPRS J. Photogramm. Remote Sens. 57, 356–370.

Hladik, C., Alber, M., 2012. Accuracy assessment and correction of a lidar-derived salt marsh digital elevation model. Remote Sens. Environ. 121, 224–235.

Höhle, J., 2009. Dem generation using a digital large-format frame camera. Photogramm. Eng. Remote. Sens. 75, 87–93.

Huising, E.J., Gomes Pereira, L.M., 1998. Errors and accuracy estimates of laser data acquired by various laser scanning systems for topographic applications. ISPRS J. Photogramm. Remote Sens. 53, 245–261.

Hunt, E.R., Hively, W.D., Fujikawa, S.J., Linden, D.S., Daughtry, C.S.T., McCarty, G.W., 2010. Acquisition of NIR-green-blue digital photographs from unmanned aircraft for crop monitoring. Remote Sens. 2, 290–305.
James, M.R., Robson, S., 2012. Straightforward reconstruction of 3D surfaces and topography with a camera: accuracy and geoscience application. J. Geophys. Res. Earth Surf. 117, F03017 (10.01029/02011JF002289).
Jenson, S.K., Domingue, J.O., 1988. Extracting topographic structure from digital elevation data for geographic information system analysis. Photogramm. Eng. Remote. Sens. 54, 1593–1600.
Jütte, K., 2008. Vergleich verschiedener low-cost Luftbildaufnahmesysteme sowie Einsatz von Drohnen: Grenzen und Möglichkeiten. Bayerische Landesanstalt für Wald und Forstwirtschaft. Der gepixelte Wald - Fachtagung zur Forstlichen Fernerkundung.
Kersten, T., Mechelke, K., Lindstaedt, M., Sternberg, H., 2008. Geometric accuracy investigation of the latest terrestrial laser scanning systems. FIG Working Week, Stockholm.
Konecny, G., 2002. Geoinformation: Remote Sensing, Photogrammetry and Geographic Information Systems, Second edition. Taylor & Francis, London.
Kung, O., Strecha, C., Beyeler, A., Zufferey, J.-C., Floreano, D., Fua, P., Gervaix, F., 2011. The accuracy of automatic photogrammetric techniques on ultra-light UAV imagery. Int. Arch. Photogramm. Remote. Sens. Spat. Inf. Sci. XXXVIII, 1–7.
Landes, T., Grussenmeyer, P., 2011. Les principes fondamentaux de la lasergrammétrie terrestre: sytèmes et caractéristiques. Revue XYZ 128, 37–49.
Lane, S.N., James, T.D., Crowell, M.D., 2000. Application of digital photogrammetry to complex topography for geomorphological research. Photogramm. Rec. 16, 793–821.
Le Bissonnais, Y., Benkhadra, H., Chaplot, V., Fox, D., King, D., Daroussin, J., 1998. Crusting, runoff and sheet erosion on silty loamy soils at various scales and upscaling from m2 to small catchments. Soil Tillage Res. 46, 69–80.
Le Bissonnais, Y., Cerdan, O., Lecomte, V., Benkhadra, H., Souchère, V., Martin, P., 2005. Variability of soil surface characteristics influencing runoff and interrill erosion. Catena 62, 111–124.
Leica Geosystems, 2008. Leica GPS1200 User Manual.
Lindsay, J.B., Creed, I.F., 2005. Removal of artefact depressions from digital elevation models: towards a minimum impact approach. Hydrol. Process. 19, 3113–3126.
Liu, J., Pattey, E., Miller, J.R., McNairn, H., Smith, A., Hu, B., 2010. Estimating crop stresses, aboveground dry biomass and yield of corn using multi-temporal optical data combined with a radiation use efficiency model. Remote Sens. Environ. 114, 1167–1177.
Lowe, D.G., 2004. Distinctive image features from scale-invariant keypoints. Int. J. Comput. Vis. 60, 91–110.
Martin, Y., Valeo, C., Tait, M., 2008. Centimetre-scale digital representations of terrain and impacts on depression storage and runoff. Catena 75, 223–233.
Martz, L.W., Garbrecht, J., 1999. An outlet breaching algorithm for the treatment of closed depressions in a raster DEM. Comput. Geosci. 25, 835–844.
Martz, L.W., Jong, E.d., 1988. CATCH: a FORTRAN program for measuring catchment area from digital elevation models. Comput. Geosci. 14, 627–640.
Mitas, L., Mitasova, H., 1999. Spatial interpolation. In: Longley, P.A., Rhind, D.W., Goodchild, M.F., Maguire, D.J. (Eds.), Geographical Information Systems: Principles, Techniques, Management and Applications. John Wiley & Sons, Chichester, pp. 481–492.
Morris, D.G., Heerdegen, R.G., 1988. Automatically derived catchment boundaries and channel networks and their hydrological applications. Geomorphology 1, 131–141.
Nelson, A., Reuter, H.I., Gessler, P., 2009. DEM production methods and sources. Geomorphometry: concepts, software, applications. Developments in Soil Science, 33, pp. 65–85.
Niethammer, U., Rothmund, S., James, M.R., Travelletti, J., Joswig, M., 2010. UAV-based remote sensing of landslide. Int. Arch. Photogramm. Remote. Sens. Spat. Inf. Sci. 38, 496–501.
Niewinski, M., 2004. Distributed Monte Carlo simulation of a dynamic expansion system. Vacuum 73, 257–261.
Palosuo, T., Kersebaum, K.C., Angulo, C., Hlavinka, P., Moriondo, M., Olesen, J.E., Patil, H.R., Ruget, F., Rumbaur, C., Takac, J., Trnka, M., Bindi, M., Caldag, B., Ewert, F., Ferrise, R., Mirschel, W., Saylan, L., Siska, B., Rötter, R., 2011. Simulation of winter wheat yield and its variability in different climates of Europe: a comparison of eight crop growth models. Eur. J. Agron. 35, 103–114.
Parratt, L.G., 1961. Probability and Experimental Errors in Science: An Elementary Survey. Wiley, New York.
Perroy, R.L., Bookhagen, B., Asner, G.P., Chadwick, O.A., 2010. Comparison of gully erosion estimates using airborne and ground-based LiDAR on Santa Cruz Island, California. Geomorphology 118, 288–300.
Peucker, T.K., Fowler, R.J., Little, J.J., Mark, D.M., 1978. The triangulated irregular network. Proceedings: American Society of Photogrammetry, Digital Terrain Models Symposium, St. Louis, Missouri, pp. 516–540.
Pierrot Deseilligny, M., Clery, I., 2011. Apero, an open source bundle adjustment software for automatic calibration and orientation of set of images. Int. Arch. Photogramm. Remote. Sens. Spat. Inf. Sci. XXXVIII, 113–124.
Planchon, O., Esteves, M., Silvera, N., Lapetite, J.-M., 2002. Microrelief induced by tillage: measurement and modelling of surface storage capacity. Catena 46, 141–157.
Rai, R.K., Upadhyay, A., Singh, V.P., 2010. Effect of variable roughness on runoff. J. Hydrol. 382, 115–127.
Reyniers, M., Maertens, K., Vrindts, E., De Baerdemaeker, J., 2006. Yield variability related to landscape properties of a loamy soil in central Belgium. Soil Tillage Res. 88, 262–273.
Rieger, W., 1998. A phenomenon-based approach to upslope contributing area and depressions in DEMs. Hydrol. Process. 12, 857–872.
Ries, J.B., Marzolff, I., 2003. Monitoring of gully erosion in the Central Ebro Basin by large-scale aerial photography taken from a remotely controlled blimp. Catena 50, 309–328.
Rodríguez-Caballero, E., Cantón, Y., Chamizo, S., Afana, A., Solé-Benet, A., 2012. Effects of biological soil crusts on surface roughness and implications for runoff and erosion. Geomorphology 145–146, 81–89.
Rosatto, H.G., Tolon-Becerra, A., Botta, G., Presutti, M.E., 2011. Runoff estimation in small rural watersheds using DEMs in North West of Argentina. Soil Tillage Res. 112, 8–17.
Rötter, R.P., Palosuo, T., Kersebaum, K.C., Angulo, C., Bindi, M., Ewert, F., Ferrise, R., Hlavinka, P., Moriondo, M., Nendel, C., Olesen, J.E., Patil, H.R., Ruget, F., Takac, J., Trnka, M., 2012. Simulation of spring barley yield in different climatic zones of Northern and Central Europe: a comparison of nine crop models. Field Crop Res. 133, 23–36.
Salvador-Blanes, S., Cornu, S., Couturier, A., King, D., Macaire, J.-J., 2006. Morphological and geochemical properties of soil accumulated in hedge-induced terraces in the Massif Central, France. Soil Tillage Res. 85, 62–77.
Sasal, M.C., Castiglioni, M.G., Wilson, M.G., 2010. Effect of crop sequences on soil properties and runoff on natural-rainfall erosion plots under no tillage. Soil Tillage Res. 108, 24–29.
Schiewe, J., 2000. Improving the integration of digital surface models. Int. Arch. Photogramm. Remote. Sens. Spat. Inf. Sci. XXXIII, 807–814.
Smith, S.E., 2005. Topographic mapping. In: Grundwald, S. (Ed.), Environmental Soil-landscape Modeling: Geographic Information Technologies and Pedometrics. CRC Press, New York, pp. 155–182.
Smith, M.J., Chandler, J., Rose, J., 2009. High spatial resolution data acquisition for the geosciences: kite aerial photography. Earth Surf. Process. Landf. 34, 155–161.
Smith, M.W., Cox, N.J., Bracken, L.J., 2011. Terrestrial laser scanning soil surfaces: a field methodology to examine soil surface roughness and overland flow hydraulics. Hydrol. Process. 25, 842–860.
Snavely, N., Seitz, S., Szeliski, R., 2008. Modeling the world from internet photo collections. Int. J. Comput. Vis. 80, 189–210.
Soille, P., 2004a. Morphological carving. Pattern Recogn. Lett. 25, 543–550.
Soille, P., 2004b. Optimal removal of spurious pits in grid digital elevation models. Water Resour. Res. 40, W12509 (10.11029/12004WR003060).
Soille, P., Gratin, C., 1994. An efficient algorithm for drainage network extraction on DEMs. J. Vis. Commun. Image Represent. 5, 181–189.
Spaan, W.P., Sikking, A.F.S., Hoogmoed, W.B., 2005. Vegetation barrier and tillage effects on runoff and sediment in an alley crop system on a Luvisol in Burkina Faso. Soil Tillage Res. 83, 194–203.
Svoray, T., Markovitch, H., 2009. Catchment scale analysis of the effect of topography, tillage and unpaved roads on ephemeral gully incision. Earth Surf. Process. Landf. 34, 1970–1984.
Taconet, O., Ciarletti, V., 2007. Estimating soil roughness indices on a ridge-and-furrow surface using stereo photogrammetry. Soil Tillage Res. 93, 64–76.
Taconet, O., Vannier, E., Le Hégarat-Mascle, S., 2010. A contour-based approach for clods identification and characterization on a soil surface. Soil Tillage Res. 109, 123–132.
Takken, I., Govers, G., Jetten, V., Nachtergaele, J., Steegen, A., Poesen, J., 2001a. Effects of tillage on runoff and erosion patterns. Soil Tillage Res. 61, 55–60.
Takken, I., Jetten, V., Govers, G., Nachtergaele, J., Steegen, A., 2001b. The effect of tillage-induced roughness on runoff and erosion patterns. Geomorphology 37, 1–14.
Taylor, J.R., 1982. An Introduction to Error Analysis: The Study of Uncertainties in Physical Measurements. University Science Book, Mill Valley.
Temme, A.J.A.M., Schoorl, J.M., Veldkamp, A., 2006. Algorithm for dealing with depressions in dynamic landscape evolution models. Comput. Geosci. 32, 452–461.
Temme, A.J.A.M., Heuvelink, G.B.M., Schoorl, J.M., Claessens, L., 2009. Geostatistical simulation and error propagation in geomorphometry. In: Hengl, T., Reuter, H.I. (Eds.), Geomorphometry: concept, software, applications. Development in Soil Science. Elsevier, Amsterdam, pp. 121–140.
Topping, J., 1962. Errors of Observation and Their Treatment. Chapman and Hall, London.
Trautner, A., Arvidsson, J., 2003. Subsoil compaction caused by machinery traffic on a Swedish Eutric Cambisol at different soil water contents. Soil Tillage Res. 73, 107–118.
U.S. Geological Survey, 1997. Standards for Digital Elevation Models, Part 1: General, Part 2: Specifications, Part 3: Quality Control. In: U.S.D.o.t. Interior (Ed.), U.S. Geological Survey, Washington, DC.
Vallet, J., Panissod, F., Strecha, C., Tracol, M., 2011. Photogrammetric performance of an ultra light weight swinglet "UAV". Int. Arch. Photogramm. Remote. Sens. Spat. Inf. Sci. XXXVIII, 1–7.
Vanmarcke, E., 1983. Random Fields: Analysis and Synthesis. MIT Press, Cambridge.
Verhoeven, G., 2008. Imaging the invisible using modified digital still cameras for straightforward and low-cost archaeological near-infrared photography. J. Archaeol. Sci. 35, 3087–3100.
Verhoeven, G., 2011. Taking computer vision aloft — archaeological three-dimensional reconstructions from aerial photographs with PhotoScan. Archaeol. Prospect. 18, 67–73.
Vozikis, G., Haring, A., Vozikis, E., Kraus, K., 2004. Laser scanning: a new method for recording and documentation in archaeology. The Olympic spirit in Surveying, Athens (Greece).
Warner, W.S., 1995. Mapping a three-dimensional soil surface with hand-held 35 mm photography. Soil Tillage Res. 34, 187–197.
Watts, D.W., Hall, J.K., 1996. Tillage and application effects on herbicide leaching and runoff. Soil Tillage Res. 39, 241–257.
Watts, A.C., Ambrosia, V.G., Hinkley, E.A., 2012. Unmanned aircraft systems in remote sensing and scientific research: classification and considerations of use. Remote Sens. 4, 1671–1692.
Webster, R., Olivier, M.A., 2007. Geostatistics for Environmental Scientists, 2nd edition.
Wechsler, S.P., 2007. Uncertainties associated with digital elevation models for hydrologic applications: a review. Hydrol. Earth Syst. Sci. 11, 1481–1500.
Wehr, A., Lohr, U., 1999. Airborne laser scanning: an introduction and overview. ISPRS J. Photogramm. Remote Sens. 54, 68–82.

Westoby, M.J., Brasington, J., Glasser, N.F., Hambrey, M.J., Reynolds, J.M., 2012. 'Structure-from-Motion' photogrammetry: a low-cost, effective tool for geoscience applications. Geomorphology 179, 300–314.
Wilson, G.V., McGregor, K.C., Boykin, D., 2008. Residue impacts on runoff and soil erosion for different corn plant populations. Soil Tillage Res. 99, 300–307.
Wolf, P.R., Dewitt, B.A., 2000. Elements of Photogrammetry with Application in GIS. McGraw-Hill, New York.
Yang, J.-L., Zhang, G.-L., Shi, X.-Z., Wang, H.-J., Cao, Z.-H., Ritsema, C.J., 2009. Dynamic changes of nitrogen and phosphorus losses in ephemeral runoff processes by typical storm events in Sichuan Basin, Southwest China. Soil Tillage Res. 105, 292–299.
Yuan, X., 2009. Quality assessment for GPS-supported bundle block adjustment based on aerial digital frame imagery. Photogramm. Rec. 24, 139–156.
Zhang, C., 2008. An UAV-based photogrammetric mapping system for road condition assessment. In: R.S.a.S.I.S. The International Archives of the Photogrammetry (Ed.), ISPRS Congress, Beijing, China, pp. 627–631.
Zhao, L., Liang, X., Wu, F., 2013. Soil surface roughness change and its effect on runoff and erosion on the Loess Plateau of China. J. Arid. Land 1–10.
Zhu, Q., Tian, Y., Zhao, J., 2006. An efficient depression processing algorithm for hydrologic analysis. Comput. Geosci. 32, 615–623.